



Apatite geochemistry of the Taihe layered intrusion, SW China: Implications for the magmatic differentiation and the origin of apatite-rich Fe-Ti oxide ores

Yu-Wei She ^{a,b}, Xie-Yan Song ^{b,*}, Song-Yue Yu ^b, Lie-Meng Chen ^b, Wen-Qin Zheng ^b

^a Laboratory of Isotope Geology, Ministry of Land and Resources, Institute of Geology, Chinese Academy of Geological Sciences, Beijing 100037, PR China

^b State Key Laboratory of Ore Deposit Geochemistry, Institute of Geochemistry, Chinese Academy of Sciences, Guiyang 550002, PR China



ARTICLE INFO

Article history:

Received 13 October 2015

Received in revised form 4 April 2016

Accepted 6 April 2016

Available online 9 April 2016

Keywords:

Apatite

Fe-Ti oxide

Fractional crystallization

Taihe layered intrusion

Emeishan large igneous province

ABSTRACT

The Taihe intrusion is one of the layered intrusions situated in the central zone of the Emeishan Large Igneous Province (ELIP), SW China. The cyclic units in the Middle Zone of the intrusion are composed of apatite-magnetite clinopyroxenite at the base and gabbro at the top. The apatite-rich oxide ores contain 6–12 modal% apatite and 20–50 modal% Fe-Ti oxides evidently distinguished from the coeval intrusions in which apatite-rich rocks are poor in Fe-Ti oxides. Most of apatites of the Taihe Middle and Upper Zones are fluorapatite, although four samples show slightly high Cl content in apatite suggesting that they crystallize from a hydrous parental magma. Compared to the apatite from the gabbro of the Panzhihua intrusion, situated 100 km to the south of the Taihe intrusion, the apatite of the Taihe rocks is richer in Sr and depleted in HREE relative to LREE. The calculated magma in equilibrium with apatite of the Taihe Middle and Upper Zones also shows weakly negative Sr anomalies in primitive mantle normalized trace element diagrams. These features indicate that the apatite of the Taihe Middle and Upper Zones crystallizes after clinopyroxene and before plagioclase. The apatite of the Taihe Middle and Upper Zones shows weakly negative Eu anomalies suggesting a high oxygen fugacity condition. The high iron and titanium contents in the oxidizing magma result in crystallization of Fe-Ti oxides. Crystallization of abundant Fe-Ti oxides and clinopyroxenes lowers the solubility of phosphorus and elevates SiO₂ concentration in the magma triggering the saturation of apatite. The positive correlations of Sr, V, total REE contents and Ce/Yb ratio in apatite with cumulus clinopyroxene demonstrate approximately compositional equilibrium between these phases suggesting they crystallized from the same ferrobasaltic magma. Early crystallization and accumulation of Fe-Ti oxide together with apatite produced the apatite-rich oxide ores at the base of the cyclic units of the Taihe Middle Zone.

© 2016 Elsevier B.V. All rights reserved.

1. Introduction

Magmatic apatite-rich Fe-Ti oxide ores are commonly associated with mafic layered intrusions or Proterozoic anorthositic complexes (Eales and Cawthorn, 1996; Ashwal, 2010; McLelland et al., 2010; Cawthorn, 2015). The Fe-Ti oxide ores varying in apatite modal content occur generally in the upper part of the layered intrusions, such as the Bushveld Complex and the Sept Iles intrusion (Von Gruenewaldt, 1993; Higgins and Doig, 1981). The Fe-Ti-P ore deposits associated with anorthosites occur generally as veins and lenses and cut enclosing rocks (Kolker, 1982; Dymek and Owens, 2001). The origin of these Fe-Ti-P ores is highly debated. Gravitational settling and sorting of crystals from ferrobasaltic magma have been proposed by a number of authors

for their formation (Duchesne, 1999; Dymek and Owens, 2001). Nevertheless, some authors argued that the dense ores resulted from immiscible Fe-Ti-P melt segregated from mafic magma (Lister, 1966; Kolker, 1982; Naslund, 1983; Reynolds, 1985).

In the central zone of the Emeishan Large Igneous Province (ELIP), several large layered intrusions, such as Panzhihua, Baima, Xinjie and Hongge, host thick layers of Fe-Ti oxide ores, in which apatite is rare (<1 modal%). The formation of the Fe-Ti oxide layers are attributed to early crystallization and gravitational accumulation of Fe-Ti oxides from Fe-Ti-enriched magmas, which are produced by fractional crystallization of high-Ti picritic magma at depths (Pang et al., 2008a, 2009; Ganino et al., 2008, 2013; Zhang et al., 2009; Bai et al., 2012; Zhang et al., 2012; Song et al., 2013; Howarth et al., 2013; Howarth and Prevec, 2013). These thick Fe-Ti oxide layers are also thought to have crystallized from a dense immiscible Fe-rich melt (Zhou et al., 2005, 2013; Shellnutt et al., 2010; Wang and Zhou, 2013; Dong et al., 2013; Xing et al., 2014). A fluid dynamic model was also proposed to explain the origin of these oxide deposits (Hou et al., 2012; Luo et al., 2014;

* Corresponding author at: State Key Laboratory of Ore Deposit Geochemistry, Institute of Geochemistry, Chinese Academy of Sciences, 46th Guanshui Road, Guiyang 550002, PR China.

E-mail address: songxieyan@vip.gyig.ac.cn (X.-Y. Song).

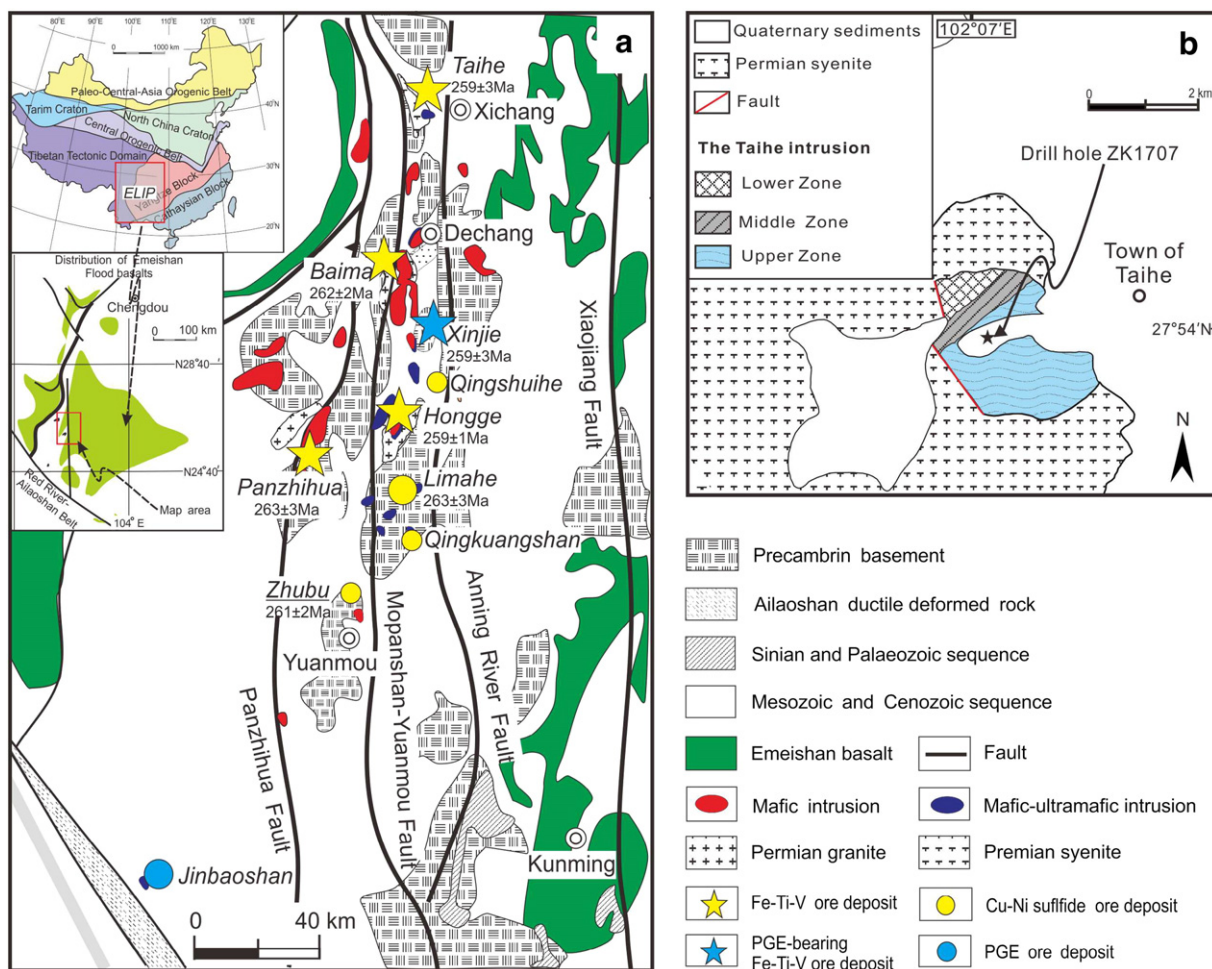


Fig. 1. (a) Regional geological map of the central Emeishan large igneous province (ELIP), showing the distribution of layered mafic-ultramafic intrusions hosting Fe-Ti oxide ore deposits (modified after Song et al., 2009). (b) Simplified geological map of the Taihe intrusion.

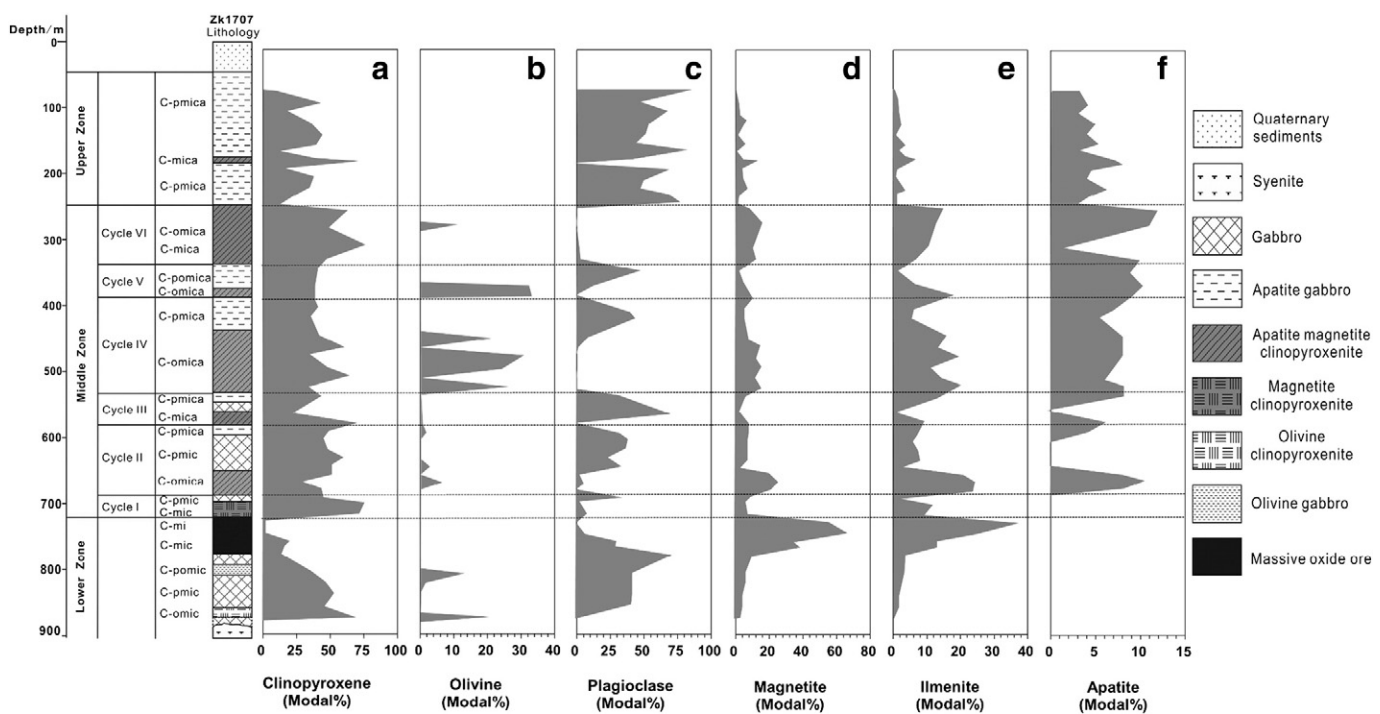


Fig. 2. Lithostratigraphic column from drill core ZK1707 from the Taihe intrusion. C = cumulus; m = magnetite; i = ilmenite; o = olivine; c = clinopyroxene; p = plagioclase; a = apatite.

Hei et al., 2015). In contrast, the Fe-Ti oxide ores in the Middle Zone of the Taihe intrusion (ELIP) are distinctive because they contain 6–12% cumulus apatites, suggesting that its parental magma is not only enriched in iron and titanium but also enriched in phosphorus. Thus, the following questions need to be addressed 1) why apatite occurs in oxide-rich rocks of the Taihe Middle Zone yet other coeval intrusions have apatite occurring only in the oxide-barren gabbro in the upper part of the intrusions; 2) does phosphorus play a direct role on the formation of Fe-Ti oxide ores of the Taihe Middle Zone?

Many minor and trace elements, such as F, Cl, REE, Th, U and Sr, are highly concentrated in apatite (Watson and Green, 1981; Webster et al., 1999; Bedard, 2001; Prowatke and Klemme, 2006). Apatite has also been shown to document the evolution of magma and petrogenesis of apatite-rich rocks (e.g. Sha and Chappell, 1999; Hoskin et al., 2000; Dymek and Owens, 2001; Belousova et al., 2001, 2002; Tollari et al., 2008; Chu et al., 2009; Miles et al., 2013). In this study, major and trace element compositions in the apatite of the Taihe Middle and Upper Zones are measured using electron microprobe and LA-ICP-MS, respectively. The new dataset can be used to constrain the magmatic differentiation processes and origin of the apatite-rich oxide ores in the Taihe Middle Zone.

2. Geological background and the Taihe intrusion

The ELIP covers an area $> 5 \times 10^5 \text{ km}^2$ in southwestern China (Fig. 1a) and is derived from a late Permian mantle plume (Chung and Jahn, 1995; Zhou et al., 2002; Xu et al., 2001). It consists of extensive Permian flood basalts and genetically associated ~260 Ma mafic-ultramafic intrusions and felsic plutons (Zhou et al., 2002, 2005, 2008; Zhong and Zhu, 2006; Xu et al., 2008; Shellnutt and Zhou, 2008; Zhong et al., 2011; Hou et al., 2013 and references therein). The ELIP can be divided into a central and an outer zone (Xu et al., 2001 and references therein). The central zone of the ELIP is characterized by low-Ti basalts overlain by high-Ti basalts, whereas the outer zone of the ELIP predominantly consists of high-Ti basalts (Xu et al., 2001). A series of Late Permian mafic-ultramafic intrusions are distributed along several N-S trending faults in the central zone of the ELIP, in an area known Pan-Xi region (Fig. 1a) (Liu et al., 1985 and references therein). Some of them host giant Fe-Ti-V oxide deposits, such as Panzhihua, Baima, Hongge, Xinjie and Taihe, as mentioned above.

The Taihe intrusion is approximately 3 km long and 2 km wide, with an exposed area of $\sim 13 \text{ km}^2$ (Fig. 1b). The layering dips to the southeast with angles of 50–60° and body have a thickness of $\sim 1.2 \text{ km}$. She et al.

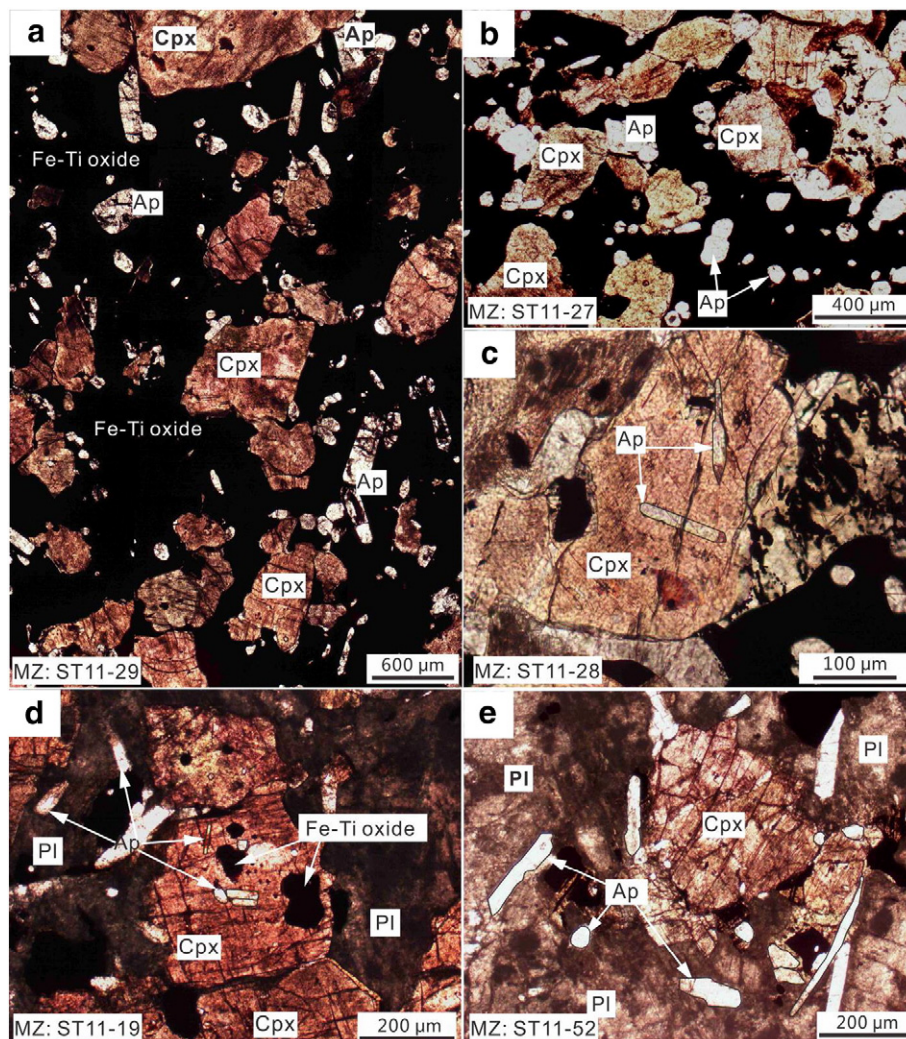


Fig. 3. Textural relationships between apatite-rich oxide ores and apatite gabbros of the Taihe MZ and UZ: (a) Euhedral apatite grains are closely associated with Fe-Ti oxides in the apatite-magnetite clinopyroxenite; (b) subhedral-euhedral cumulus apatite crystals among Fe-Ti oxides and clinopyroxene in the apatite-magnetite clinopyroxenite; (c) euhedral columnar apatite is enclosed in clinopyroxene in the apatite-magnetite clinopyroxenite; (d) subhedral-euhedral apatite and Fe-Ti oxides are enclosed in clinopyroxene in the apatite gabbro; (e) subhedral-euhedral cumulus apatites are enclosed in plagioclase of the apatite gabbro. Cpx = clinopyroxene; Pl = plagioclase; Ap = apatite; Fe-Ti oxide = magnetite and ilmenite. LZ = lower zone; MZ = middle zone; UZ = upper zone.

(2014) determined the SHRIMP zircon age of 259 ± 3 Ma on the Taihe gabbro which is consistent with the mantle plume activities. The Taihe intrusion is completely surrounded by a contemporaneous syenite pluton (Xu et al., 2008). The presence of syenite dykes with thicknesses of several meters in the Taihe intrusion, indicate that the syenite formed slightly later. Based on mineral assemblages and lithologic textures, the Taihe layered intrusion can be divided into Lower Zone (LZ), Middle Zone (MZ) and Upper Zone (UZ) (Fig. 2). The LZ is defined by the occurrence of apatite-free massive Fe-Ti oxide layers, MZ is characterized by containing as high as 6–12 modal% apatite in the disseminated oxide ores, and the UZ is marked by the occurrence of oxide-barren apatite gabbro.

The LZ is composed of olivine clinopyroxenite, olivine gabbro, gabbro and massive Fe-Ti oxide ore from the base to the top (Fig. 2). The olivine clinopyroxenite contains 60–80 modal% clinopyroxene, 20–

30 modal% olivine, <8 modal% plagioclase and <5 modal% Fe-Ti oxides. As plagioclase content increases to 40–70 modal%, the rock changes to gabbro. The massive Fe-Ti oxide ore at the top of the LZ is composed predominantly of 50–90 modal% Fe-Ti oxides (including 40–70 modal% magnetite and 13–40 modal% ilmenite) and variable amounts of clinopyroxene and plagioclase (<50 modal%). The MZ has six cyclic units (Cycles I–VI) and each unit dominantly consists of apatite-magnetite clinopyroxenite and gabbro from the base to the top with exception of Cycle I, which consists of magnetite clinopyroxenite and gabbro (Fig. 2). The apatite-magnetite clinopyroxenite consists of 30–70% clinopyroxene, 20–50 modal% Fe-Ti oxides, 6–12 modal% apatite and <10 modal% plagioclase, locally up to 25 modal% olivine. The gabbro comprising the upper part of the cyclic units contains 12–70 modal% plagioclase, 25–60 modal% clinopyroxene and 5–20 modal% Fe-Ti oxides. As apatite content increases to 5–8 modal%, the rock changes to

Table 1
Modal content of minerals of the Taihe intrusion.

Sample	Depth (m)	Rock	Zone	Cyclic unit	OI	Cpx	Hbl	Pl	Ap	Mt	IIm	Sul
T11-59	63	Ap Gab	UZ		0	10	0	85	3	1	1	0
ST11-58	81	Ap Gab	UZ		0	43	4	46	4	2	1	<1
ST11-57	98	Ap Gab	UZ		0	20	8	66	3	2	1	0
ST11-56	113	Ap Gab	UZ		0	35	0	52	5	6	2	0
ST11-55	130	Ap Gab	UZ		0	43	0	50	4	2	1	0
ST11-54	146	Ap Gab	UZ		0	40	1	45	5	5	4	0
ST11-53	154	Ap Gab	UZ		0	12	1	81	3	2	1	0
ST11-52	169	Ap Gab	UZ		0	38	3	42	7	6	4	<1
ST11-51	173	Ap Mt Cpx	UZ		0	71	1	0	8	13	7	<1
ST11-50	185	Ap Gab	UZ		0	20	1	70	4	4	1	0
ST11-49	198	Ap Gab	UZ		0	41	1	50	4	3	1	0
ST11-48	216	Ap Gab	UZ		0	33	1	50	6	6	4	0
ST11-47	226	Ap Gab	UZ		0	26	1	66	4	2	1	0
ST11-01	236	Ap Gab	UZ		0	15	1	77	3	3	1	0
ST11-02	246	Ap Mt Cpx	MZ	VI	0	65	0	0	12	8	15	<1
ST11-03	270	Ap Mt Cpx	MZ	VI	8	50	1	0	11	16	13	1
ST11-05	305	Mt Cpx	MZ	VI	0	74	3	1	2	10	10	<1
ST11-06	323	Ap Mt Cpx	MZ	VI	0	49	20	0	10	12	8	1
ST11-07	342	Ap Gab	MZ	V	0	40	0	46	9	3	2	<1
ST11-08	363	Ap Gab	MZ	V	26	40	1	12	10	5	6	<1
ST11-09	381	Ap Mt Cpx	MZ	V	24	38	1	0	9	10	18	<1
ST11-10	400	Ap Gab	MZ	IV	0	40	1	39	7	6	7	<1
ST11-11	415	Ap Gab	MZ	IV	0	36	5	42	5	6	6	<1
ST11-13	443	Ap Mt Cpx	MZ	IV	16	43	1	8	8	8	16	<1
ST11-14	459	Ap Mt Cpx	MZ	IV	0	62	1	1	8	15	13	<1
ST11-15	471	Ap Mt Cpx	MZ	IV	24	35	1	0	8	12	20	<1
ST11-16	490	Ap Mt Cpx	MZ	IV	18	48	0	0	7	16	11	<1
ST11-17	506	Ap Mt Cpx	MZ	IV	0	66	1	1	6	12	14	<1
ST11-18	517	Ap Mt Cpx	MZ	IV	20	35	0	1	8	16	20	<1
ST11-19	534	Ap Gab	MZ	III	0	42	0	30	8	7	13	<1
ST11-20	558	Gab	MZ	III	0	25	1	70	0	2	2	<1
ST11-21	575	Ap Mt Cpx	MZ	III	0	70	4	0	6	9	9	2
ST11-22	589	Gab	MZ	II	1	46	2	32	4	8	7	<1
ST11-23	602	Gab	MZ	II	0	46	3	38	0	7	6	<1
ST11-24	616	Gab	MZ	II	0	50	1	35	0	7	7	<1
ST11-25	629	Gab	MZ	II	0	60	1	24	0	7	8	<1
ST11-26	641	Gab	MZ	II	2	50	5	35	0	5	3	<1
ST11-27	653	Ap Mt Cpx	MZ	II	0	51	1	0	8	19	21	<1
ST11-28	665	Ap Mt Cpx	MZ	II	5	30	2	4	10	24	25	<1
ST11-29	677	Ap Mt Cpx	MZ	II	0	43	5	0	8	20	24	<1
ST11-30	688	Gab	MZ	I	0	46	3	36	0	10	2	3
ST11-32	698	Mt Cpx	MZ	I	0	74	2	1	0	8	12	3
ST11-33	714	Mt Cpx	MZ	I	0	72	1	8	0	9	10	<1
ST11-34	728	Ore	LZ		0	3	0	1	0	56	37	3
ST11-35	744	Ore	LZ		0	3	0	5	0	67	25	<1
ST11-39	756	Ore	LZ		0	20	1	28	0	38	13	<1
ST11-40	765	Ore	LZ		0	18	1	28	0	40	13	<1
ST11-41	780	Gab	LZ		0	15	0	71	0	10	4	<1
ST11-42	804	Ol Gab	LZ		10	37	1	40	0	8	4	<1
ST11-43	820	Gab	LZ		1	48	1	40	0	7	3	<1
ST11-44	839	Gab	LZ		0	52	1	41	0	4	2	<1
ST11-45	854	Gab	LZ		0	45	6	40	0	5	2	2
ST11-46	871	Ol Cpx	LZ		16	68	2	8	0	4	1	1

OI = olivine; Cpx = clinopyroxene; Hbl = hornblende; Pl = plagioclase; Ap = apatite; Mt = magnetite; IIm = ilmenite; Gab = gabbro; Ap Gab = apatite gabbro; Ol Gab = olivine gabbro; Mt Cpx = magnetite clinopyroxenite; Ap Mt Cpx = apatite-magnetite clinopyroxenite; Ol Cpx = olivine clinopyroxenite; Ore = massive Fe-Ti oxide ore; UZ = upper zone; MZ = middle zone; LZ = lower zone.

apatite gabbro. The UZ of the Taihe intrusion is composed of apatite gabbro and a thin interlayer of apatite-magnetite clinopyroxenite (Fig. 2). The apatite gabbro contains 42–85 modal% plagioclase and 10–40 modal% clinopyroxene, and 5–8 modal% apatite and <10 modal% Fe-Ti oxide.

Apatite grains from the apatite-magnetite clinopyroxenite in the lower part of cyclic units of the MZ occur as subhedral to euhedral and have 100 to 300 μm in length (up to 700 μm). In these disseminated ores, apatite and Fe-Ti oxides are always closely associated and occupy the interstitial regions between silicate minerals (Fig. 3a–b). Small amounts of apatite grains with euhedral prismatic crystal are enclosed in clinopyroxene grains (Fig. 3c). Apatite from the gabbro displays subhedral to euhedral grains with 100–150 μm in length. Many apatite grains are closely associated with Fe-Ti oxides. Some euhedral apatite crystals are partially or completely enclosed in the clinopyroxene or plagioclase grains (Fig. 3d–e). Fe-Ti oxides show an anhedral texture and have an interstitial habit along with apatite (Fig. 3a–b). The texture relationship is probably resulted from sub-solidus grain boundary migration (Duchesne, 1999; Pang et al., 2008a, 2008b). Some euhedral Fe-Ti oxide crystals have locally been observed as inclusions in silicate minerals (Fig. 3d). Clinopyroxene is generally subhedral to euhedral with schiller structure represented by exsolution of oxide lamellae parallel along two intersecting planes. Some clinopyroxene grains contain euhedral apatite and Fe-Ti oxide crystals (Fig. 3c–d). Olivine appears locally as subhedral to poikilitic grains. Some surrounded olivine is enclosed in larger clinopyroxene grains. Plagioclase occurs as tabular subhedral grains in the clinopyroxenite, and as larger platy grains in the gabbro.

3. Samples and analytical methods

In this study, 53 samples were collected from an exploration drill hole (ZK1707) of the Taihe intrusion (Fig. 1b) and were used to constrain modal proportions in each cyclic unit (Table 1). We chose 26 samples from this drill hole to analyze the major and trace elements of apatite in the thin sections from the Taihe MZ and UZ.

The major element compositions of apatite were determined by wavelength dispersive X-ray analysis using a JEOL EPMA-1600 electron microprobe at the State Key Laboratory of Ore Deposit Geochemistry, Institute of Geochemistry, Chinese Academy of Science. An acceleration voltage of 25 kV, a beam current of 10 nA and a beam size of 10 μm diameter were applied to all element analyses for apatite (Goldoff et al., 2012). Analytical reproducibility was within 2%. The accuracy of analysis was monitored using mineral standards: apatite for Ca, P and F, tugtupite for Cl, albite for Na, pyrope for Mn and magnetite for Fe.

Trace elements in apatite were determined by laser ablation inductively coupled-plasma mass spectrometry (LA-ICP-MS) at the State Key Laboratory of Ore Deposit Geochemistry, Institute of Geochemistry, Chinese Academy of Sciences. Laser analysis of apatite was performed by a GeoLasPro laser-ablation system on thin sections. Ion-signal intensities were acquired through an Agilent 7700x ICP-MS instrument with Helium (He) as the carrier gas. Ablation protocol employed a spot diameter of 44 μm at 4 Hz repetition rate for 40 s (equating to 160 pulses) in this study. Each analysis incorporated a background acquisition for approximately 14 s (gas blank) followed by 35 s of data acquisition. The international standards NIST SRM 610, BCR-2G, BIR-1G and BHVO-2G (from USGS) were used as external calibration for the apatite *in situ* analysis. MPI-DING basaltic glasses: KL2-G and ML3B-G (prepared by Max-Planck-Institute für Chemie, Mainz, Germany) were treated as unknown samples to test the accuracy and precision of the LA-ICP-MS method. Data reduction was performed using an ICPMSDataCal software (Liu et al., 2008). Measured values of reference glasses agree well with the recommended values of these standards, and precision is higher than 5% for most of the elements (Table 2). The preferred values of element concentrations for these reference glasses are from the GeoReM dataset (<http://georem.mpch-mainz.gwdg.de>). The major and trace elemental compositions of the apatite in each sample are listed in Table 3.

4. Major and trace elemental compositions of the apatite

The apatite in Cycles II–V of the Taihe MZ has 1.98–4.24 wt% F and 0.10–0.36 wt% Cl. It should be noted that the apatite of Cycles I and VI of the Taihe MZ has 0.15–1.47 wt% Cl, and 1.71–2.82 wt% F (Table 3). In the Taihe UZ, the apatite has 2.46–2.85 wt% F and 0.18–0.40 wt% Cl, which is similar in composition to those of most of samples in the Taihe MZ (Table 3). F content of the apatite shows small variations in the stratigraphic levels (Fig. 4a). In contrast, a remarkable reversal of Cl of apatite is recognized in Cycle VI (Fig. 4b). The end member F-Cl-OH compositions in most of apatites of the Taihe MZ and UZ plot in the field of apatite from the Panzhihua and Skeargard intrusions, whereas several samples show slightly high Cl content in apatite (Fig. 5). There is a roughly negative correlation between Cl and F in the apatite with higher Cl (Fig. 6a). Most of fluorapatite in the Taihe MZ and UZ has lower F/Cl ratio, which is positively correlated with F content (Fig. 6b).

Table 2

Comparison of measured and recommended values for the compositions of standards KL2-G and ML3B-G.

Sample	KL2-G			ML3B-G		
	Tholeiitic basalt from Kilauea		RSD	Tholeiitic basalt from Mauna Loa		RSD
Rock	Accepted values	Average value (19)		Accepted values	Average value (19)	
Major elements (wt%)						
SiO ₂	50.30	50.56	0.14	51.40	51.69	0.16
TiO ₂	2.56	2.60	0.04	2.13	2.13	0.04
Al ₂ O ₃	13.30	13.48	0.08	13.60	13.81	0.06
FeO(t)	10.70	10.91	0.14	10.90	11.09	0.14
MnO	0.17	0.17	0.00	0.17	0.18	0.00
MgO	7.34	7.33	0.05	6.59	6.58	0.06
CaO	10.90	11.16	0.09	10.50	10.71	0.11
Na ₂ O	2.35	2.36	0.03	2.40	2.42	0.03
K ₂ O	0.48	0.49	0.01	0.39	0.39	0.01
P ₂ O ₅	0.23	0.24	0.01	0.23	0.24	0.01
Trace elements (ppm)						
Mn	1278.17	1339.71	0.00	1316.90	1372.49	0.00
Sc	31.80	34.09	1.33	31.60	32.38	1.38
V	309.00	317.54	1.98	268.00	288.22	2.83
Cr	294.00	288.47	12.98	177.00	160.21	3.73
Co	41.20	43.73	0.91	41.20	43.42	0.82
Ni	112.00	112.95	3.11	107.00	109.19	2.60
Cu	87.90	92.18	5.08	112.00	120.99	6.47
Zn	110.00	106.03	3.61	108.00	105.65	4.94
Ga	20.00	19.86	0.68	19.60	18.52	0.65
Rb	8.70	8.37	0.34	5.80	5.70	0.22
Sr	356.00	363.59	4.56	312.00	316.64	3.53
Y	25.40	25.12	0.95	23.90	23.64	0.87
Zr	152.00	157.26	3.17	122.00	125.22	2.91
Nb	15.00	14.48	0.42	8.61	8.04	0.24
Ba	123.00	123.78	2.31	80.10	80.39	2.18
La	13.10	13.48	0.32	8.99	9.08	0.17
Ce	32.40	33.48	0.62	23.10	23.49	0.47
Pr	4.60	4.78	0.16	3.43	3.42	0.18
Nd	21.60	22.35	1.03	16.70	17.32	0.93
Sm	5.54	5.66	0.42	4.75	4.96	0.46
Eu	1.92	2.08	0.17	1.67	1.73	0.11
Gd	5.92	6.17	0.50	5.26	5.35	0.53
Tb	0.89	0.92	0.08	0.80	0.82	0.08
Dy	5.22	5.44	0.35	4.84	4.90	0.35
Ho	0.96	1.02	0.08	0.91	0.94	0.07
Er	2.54	2.74	0.30	2.44	2.62	0.24
Tm	0.33	0.36	0.04	0.32	0.32	0.04
Yb	2.10	2.26	0.30	2.06	2.15	0.21
Lu	0.29	0.31	0.03	0.29	0.28	0.04
Hf	3.93	3.96	0.31	3.22	3.28	0.27
Ta	0.96	0.84	0.05	0.56	0.47	0.04
Pb	2.07	1.87	0.18	1.38	1.31	0.11
Th	1.02	0.93	0.09	0.55	0.48	0.04
U	0.55	0.64	0.11	0.44	0.53	0.08

The basaltic glasses (KL2-G and ML3B-G) were prepared by Max-Planck-Institute für Chemie, Mainz, Germany (<http://georem.mpch-mainz.gwdg.de>).

Table 3
Representative analyses of major and trace element compositions of apatite from the Taihe intrusion.

Sample	ST11-58	ST11-56	ST11-52	ST11-51	ST11-48	ST11-02	ST11-03	ST11-05	ST11-06	ST11-08	ST11-09	ST11-10	ST11-11	ST11-13
Depth (m)	81	113	169	173	216	246	270	305	323	363	381	400	415	443
Rock	Ap Gab	Ap Gab	Ap Gab	Ap Mt Cpx	Ap Gab	Ap Mt Cpx	Ap Mt Cpx	Mt Cpx	Ap Mt Cpx	Ap Gab	Ap Mt Cpx	Ap Gab	Ap Gab	Ap Mt Cpx
Zone	UZ	UZ	UZ	UZ	UZ	MZ	MZ	MZ	MZ	MZ	MZ	MZ	MZ	MZ
Cyclic unit					VI	VI	VI	VI	V	V	IV	IV	IV	IV
Number	5	5	5	4	4	4	4	5	6	5	4	5	5	4
Major oxide (wt%)														
CaO	54.13	54.01		53.95	54.31	53.97	54.18	54.22	53.61	53.40	53.89	54.07		53.98
P ₂ O ₅	43.54	43.90		43.69	44.05	43.58	43.42	43.63	43.40	43.22	43.72	43.87		43.67
FeO	0.11	0.17		0.33	0.09	0.07	0.10	0.02	0.08	0.35	0.13	0.15		0.16
MnO	0.04	0.03		0.02	0.05	0.01	0.02	0.01	0.04	0.03	0.01	0.05		0.03
Na ₂ O	0.00	0.01		0.00	0.01	0.01	0.04	0.00	0.01	0.01	0.02	0.01		0.02
F	2.85	2.63		2.46	2.80	2.82	2.76	2.31	2.68	4.24	2.81	2.37		3.36
Cl	0.40	0.18		0.24	0.27	0.15	0.51	0.73	1.22	0.13	0.14	0.15		0.10
F=O	1.20	1.11		1.04	1.18	1.19	1.16	0.97	1.13	1.78	1.18	1.00		1.42
Cl=O	0.09	0.04		0.05	0.06	0.03	0.11	0.17	0.28	0.03	0.03	0.03		0.02
Total	99.10	99.26		99.09	99.74	98.86	99.03	99.03	98.53	98.83	98.98	99.18		99.30
Trace elements (ppm)														
Sc	0.34	0.28	0.42	0.43	0.43	0.36	0.29	0.26	0.21	0.55	0.38	0.28	0.38	0.54
V	22.69	31.91	24.33	28.94	23.28	26.26	66.50	27.62	21.92	24.18	23.33	17.80	13.71	22.75
Ga	2.58	3.09	3.01	3.23	2.73	2.52	2.45	4.01	3.24	3.13	3.29	3.27	3.94	4.58
Rb	0.29	0.08	0.04	0.05	0.03	0.02	0.06	0.61	0.12	0.04	0.03	0.08	0.20	0.16
Sr	1495	1618	2211	2395	2132	2788	2957	2206	3802	1964	1995	1535	1711	1760
Y	212	258	223	266	213	189	158	231	209	228	234	188	203	248
Zr	4.94	3.84	3.03	3.69	3.31	1.91	1.59	3.15	1.65	1.83	2.40	1.94	2.60	2.22
Nb	0.03	0.01	0.03	0.03	0.02	0.01	0.04	0.03	0.03	0.01	0.03	0.01	0.04	0.01
Ba	2.10	5.03	3.23	8.68	2.60	0.20	4.96	3.89	2.35	4.37	3.42	2.52	2.29	2.87
La	268	328	334	382	253	301	225	383	365	255	272	272	244	265
Ce	699	852	847	957	684	739	582	897	865	698	734	711	647	760
Pr	105	129	124	142	107	106	91	127	123	114	116	107	99	123
Nd	556	693	649	734	590	566	509	664	640	641	650	582	544	686
Sm	112	137	123	147	122	107	100	123	118	133	133	114	111	145
Eu	31.73	40.41	38.49	44.83	39.64	32.79	33.63	36.57	34.73	39.14	39.51	34.59	34.09	39.45
Gd	100	128	112	132	112	97	92	116	106	122	122	102	102	133
Tb	11.31	13.63	11.70	13.62	11.36	10.08	9.55	11.67	10.92	13.60	13.71	10.15	10.76	13.31
Dy	48.88	63.41	54.53	65.05	53.29	46.83	41.96	54.63	51.27	58.74	59.67	47.84	51.92	63.80
Ho	7.86	10.26	8.59	10.85	8.82	8.39	7.40	9.97	8.95	8.87	9.13	7.78	8.50	10.37
Er	16.26	25.42	21.69	23.18	17.90	14.82	12.37	21.43	19.18	20.08	21.22	17.02	19.01	22.43
Tm	1.84	2.21	1.87	2.32	1.71	1.61	1.26	1.93	1.64	1.71	1.87	1.50	1.71	2.20
Yb	7.87	11.42	9.37	10.51	7.82	8.05	6.07	9.36	7.78	9.06	9.91	7.86	9.59	9.11
Lu	1.05	1.48	1.18	1.45	1.02	0.94	0.62	1.15	0.99	1.04	1.20	0.94	1.14	1.17
Hf	0.08	0.04	0.02	0.03	0.03	0.02	0.03	0.03	0.02	0.02	0.02	0.02	0.02	0.02
Ta	0.00	0.00	0.00	0.00	0.01	0.00	0.00	0.01	0.00	0.01	0.01	0.00	0.00	0.02
Th	5.84	4.95	4.47	4.28	2.43	3.77	1.55	10.21	4.04	2.21	3.00	3.88	3.79	2.77
U	1.87	1.44	1.51	1.61	0.76	1.11	0.25	4.11	1.49	0.66	0.79	1.00	1.24	0.94

Table 3 (continued)

Sample	ST11-14	ST11-15	ST11-17	ST11-18	ST11-19	ST11-21	ST11-23	ST11-26	ST11-27	ST11-28	ST11-29	ST11-32
Depth (m)	459	471	506	517	534	575	589	641	653	665	677	698
Rock	Ap Mt Cpx	Ap Mt Cpx	Ap Mt Cpx	Ap Mt Cpx	Ap Gab	Ap Mt Cpx	Ap Gab	Gab	Ap Mt Cpx	Ap Mt Cpx	Ap Mt Cpx	Mt Cpx
Zone	MZ	MZ	MZ	MZ	MZ	MZ	MZ	MZ	MZ	MZ	MZ	MZ
Cyclic unit	IV	IV	IV	IV	III	III	II	II	II	II	II	I
Number	6	4	5	5	5	5	4	4	5	5	5	4
Major oxide (wt%)												
CaO	54.40	54.77	54.77	54.82	55.30	54.07	55.28	55.69	54.99	54.91	54.68	
P ₂ O ₅	43.58	43.11	43.68	43.32	43.26	43.77	43.38	43.44	43.65	43.68	43.68	44.12
FeO	0.19	0.14	0.24	0.09	0.10	0.16	0.15	0.36	0.19	0.12	0.11	
MnO	0.01	0.04	0.03	0.04	0.03	0.03	0.04	0.01	0.02	0.02	0.02	0.02
Na ₂ O	0.01	0.01	0.01	0.01	0.02	0.01	0.02	0.01	0.01	0.01	0.01	0.01
F	2.82	2.73	2.88	2.74	2.91	1.98	2.03	2.59	2.88	3.28	1.71	
Cl	0.30	0.13	0.12	0.16	0.15	0.30	0.36	0.13	0.10	0.12	0.12	1.47
F=O	1.19	1.15	1.21	1.16	1.23	0.83	0.85	1.09	1.21	1.38	0.72	
Cl=O	0.07	0.03	0.03	0.04	0.03	0.07	0.08	0.03	0.02	0.03	0.03	0.33
Total	99.45	99.25	99.97	99.48	99.97	98.95	99.80	100.63	100.08	100.14	99.99	
Trace elements (ppm)												
Sc	0.31	0.26	0.33	0.62	0.37	0.49	0.56	0.31	0.60	0.33	0.51	0.16
V	25.45	15.31	18.06	26.01	33.11	27.98	34.37	34.97	36.96	25.43	40.72	30.46
Ga	3.73	4.74	5.36	4.37	3.44	3.16	2.89	5.24	4.31	4.54	3.19	3.43
Rb	0.09	0.04	0.07	0.04	0.06	0.15	0.06	0.10	0.05	0.12	0.15	0.13
Sr	1856	1658	1839	1673	1402	1681	1584	1410	1528	2238	1714	1322
Y	235	262	282	246	247	227	173	228	161	239	166	183
Zr	2.52	2.69	3.10	2.17	3.65	3.98	3.36	4.35	2.38	3.25	3.48	2.23
Nb	0.01	0.01	0.00	0.01	0.02	0.02	0.05	0.02	0.02	0.04	0.09	0.02
Ba	3.42	2.32	2.89	3.28	2.86	3.32	5.16	1.56	4.25	3.22	5.14	0.18
La	250	298	337	254	294	241	191	500	193	302	219	244
Ce	701	812	885	697	783	637	502	1083	512	829	585	625
Pr	115	130	134	113	122	102	78	145	79	129	88	97
Nd	636	708	735	638	654	564	429	709	441	701	465	521
Sm	137	151	148	133	136	123	91	131	92	144	93	105
Eu	38.95	40.86	42.80	36.88	36.45	36.95	28.70	36.29	27.24	49.92	26.98	29.84
Gd	129	139	139	125	126	114	88	119	87	129	84	95
Tb	12.59	13.78	13.97	12.78	14.18	13.10	9.96	12.43	9.22	14.15	9.50	10.06
Dy	61.33	67.60	68.74	60.22	62.52	57.03	43.71	56.85	41.31	61.40	41.78	46.54
Ho	9.32	10.58	11.10	9.41	9.10	9.22	7.00	8.68	6.22	10.50	7.14	7.58
Er	21.02	23.88	23.85	20.36	20.02	21.92	16.64	20.93	14.31	21.71	14.83	16.46
Tm	1.89	2.11	2.31	1.94	2.05	2.25	1.74	1.91	1.24	2.09	1.55	1.36
Yb	9.90	10.93	12.37	10.31	9.86	10.95	8.20	9.70	6.05	10.60	8.09	7.94
Lu	0.98	1.18	1.71	1.30	1.37	1.25	0.91	1.25	0.73	1.09	0.84	0.83
Hf	0.02	0.01	0.00	0.04	0.01	0.04	0.04	0.03	0.03	0.03	0.04	0.02
Ta	0.00	0.01	0.00	0.00	0.01	0.01	0.01	0.01	0.00	0.01	0.04	0.01
Th	3.61	3.70	4.51	2.62	3.86	4.01	2.59	23.83	2.67	4.24	3.73	5.69
U	0.93	0.98	1.18	0.75	1.04	0.98	0.69	6.27	0.61	0.89	1.09	1.54

The apatite from the Taihe MZ and UZ has total REE contents ranging from 1495 to 2835 ppm (Table 3) and show stratigraphic compositional reversals. The total REE contents for the apatite decrease from the base upwards in the Cycles II, IV, and VI of the MZ and Taihe UZ (Fig. 4c). Sr content in the apatite from the MZ and UZ vary widely from 1322 to 3802 ppm (Table 3). Two major reversals in Sr of apatite are present at the base of the Cycle VI of the MZ and Taihe UZ, although other stratigraphic levels only have small variations of Sr content in apatite (Fig. 4d). The V content in the apatite varies narrowly from 14 to 41 ppm (except one sample) throughout the Taihe MZ and UZ (Table 3). In the Cycles II and IV of the MZ, V content in apatite slightly decreases upwards (Fig. 4e).

Apatite of the Taihe MZ and UZ has very high ratio of La/Yb which is positively correlated with total REE contents (Fig. 7a). It is also noted that the apatite from the Taihe MZ and UZ has similar total REE contents and Sm/Yb ratio with those of the Panzhihua intrusion (Fig. 7a–b). The ratios of La/Yb and Sr/Y of the apatite in the Taihe MZ and UZ are positively correlated with Sr content, respectively (Fig. 7c–d). The Sr, V and total REE concentrations and Ce/Yb ratio of the apatite are positively correlated with those of the clinopyroxene in the Taihe MZ and UZ (Fig. 8).

Apatite from the Taihe MZ and UZ has similar chondrite-normalized REE patterns (Fig. 9). They are strongly enriched in LREE relative to HREE with La/Yb ratios ranging from 22 to 52, which are also evidently higher than the La/Yb ratios (20–27) for the Panzhihua apatite (Xing et al., 2014). Most of apatite grains from the Taihe MZ and UZ have

weakly negative Eu anomalies with Eu/Eu* values ranging from 0.84 to 0.98 and two high outliers of 1.06 and 1.11 at the apatite-magnetite clinopyroxenites of the Cycles II and V (Fig. 9).

5. Discussion

5.1. Volatiles of parental magma

Apatite is a sensitive indicator of volatile compositions in layered intrusions (Boudreau et al., 1986). The extremely Cl-rich apatite is found in the lower part of some layered intrusions, such as the Bushveld Complex in South Africa and Stillwater Complex in Montana (Boudreau et al., 1986). The apatite is rare and occurs exclusively as an irregularly interstitial phase (Boudreau et al., 1986; Boudreau and McCallum, 1989). Boudreau and McCallum (1989) suggested that the Cl-rich apatite crystallized from a “Cl-rich fluids” that exsolved from late-stage liquids in closed system. Moreover, metasomatic reaction between apatite and “Cl-rich fluids” migrated from underlying rocks also could result in extremely high Cl concentration in apatite (Willmore et al., 2000). Fig. 5 shows end-member F-Cl-OH composition of the apatite from the Taihe MZ and UZ, which is distinct significantly from the metasomatic chlorapatite of the Stillwater and Bushveld below PGE reefs (Boudreau et al., 1995). On the other hand, the composition of most of apatites from the Taihe MZ and UZ is approximately comparable with fluorapatite from the Panzhihua, Sept Iles and Skeargaard layered intrusions and the Upper Zone of the Bushveld Complex (Nash, 1976; Tollari

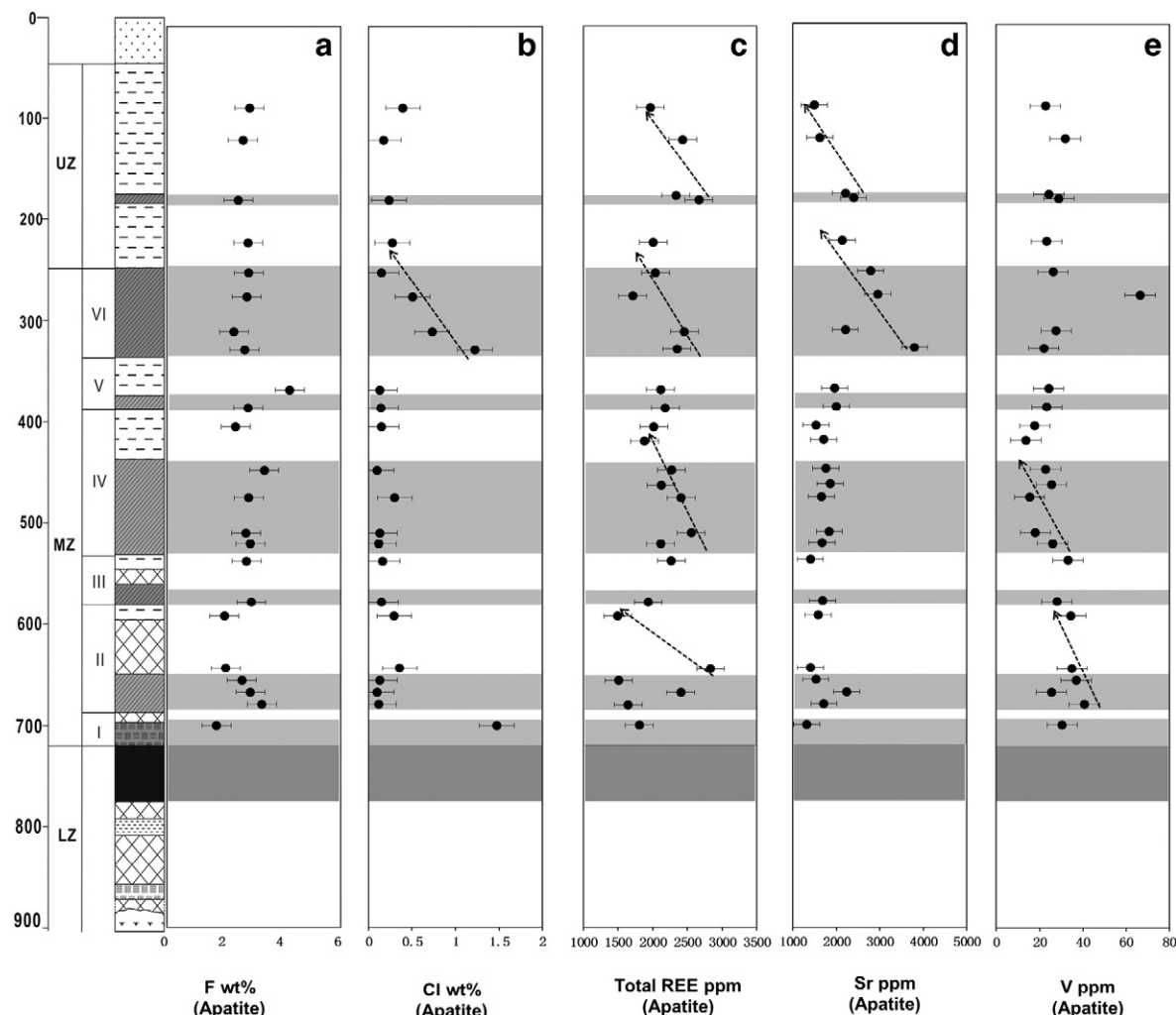


Fig. 4. Stratigraphic variations in apatite compositions of the Taihe MZ and UZ.

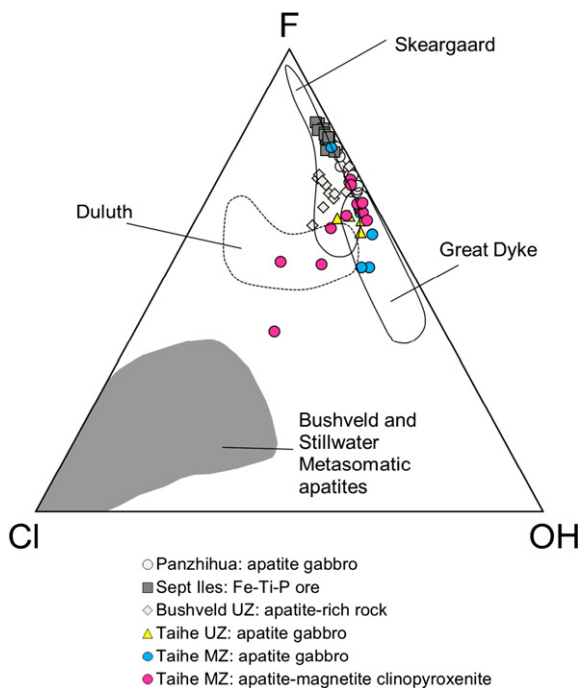


Fig. 5. End-member F, Cl and OH compositions of apatite from the Taihe MZ and UZ. The data of apatite from the Panzhihua, the Sept Iles and the Bushveld intrusions are from Xing et al. (2014); Tollari et al. (2008), and VanTongeren and Mathez (2012), respectively. Reference fields are after Boudreau et al. (1995).

et al., 2008; VanTongeren and Mathez, 2012; Xing et al., 2014). Furthermore, the apatite from the Taihe MZ and UZ occurs generally as subhedral to euhedral crystals (Fig. 3). Some euhedral apatite crystals are partially or completely enclosed in the silicate minerals (Fig. 3c–e). It suggests that they were saturated at early-stage of the magma evolution and were not the products of crystallization of trapped liquid. These features indicate that most of apatites of the Taihe MZ and UZ are typical fluorapatite and reflecting the primary cumulus compositions although one sample in Cycle I and three samples in Cycle VI of the Taihe MZ have slightly high Cl content in apatite (Fig. 4b and Fig. 5). There is no evidence to support the presence of a “Cl-rich fluid” migrated from the lower part of the Taihe intrusion because most of apatites of the MZ have very low Cl content. Due to absence of metasomatic minerals associated with apatite (Fig. 3), the slightly high Cl in the apatites of the Taihe MZ cannot be ascribed to metasomatic reaction with “Cl-rich fluid”.

The Cl variation in apatite is a function of varying Cl concentration and water fugacity within the magma from which they crystallized (Treloar and Colley, 1996; Webster et al., 1999). Experimental studies show F is easily retained in the melt phase, whereas the Cl is preferentially partitioned into the H₂O-rich fluid phase (Webster et al., 1999; Webster and DeVivo, 2002; Mathez and Webster, 2005). If apatite crystallizes from a hydrous magma, it would be expected to be enriched in Cl due to high water fugacity. The roughly negative correlation between F and Cl in apatite from the four samples of the Taihe MZ suggests that the apatite may crystallize from the hydrous parental magma (Fig. 6a). High water fugacity elevates Cl content of the magma from which the apatite crystallized. The low F/Cl ratio in the apatite also indicates a wet parental magma with relatively high Cl content (Fig. 6b). Therefore, the apatite with slightly high Cl content in the Taihe MZ may have resulted from high water content in the magma. Furthermore, a hydrous magma would be expected to crystallize plagioclase with high anorthite content ($An > 70$) due to water which can substantially depress liquidus temperatures of plagioclase (Sisson and Grove, 1993; Botcharnikov et al., 2008). The high An contents ($An = 78\text{--}86$) in plagioclase from the Taihe LZ strongly suggest that the magma is H₂O-enriched at

early-stage of differentiation (She et al., 2014). Although the rocks of the Taihe MZ and UZ have relatively Na-rich plagioclase ($An = 53\text{--}67$, She et al., 2014), this is because the volatile-rich magma was displaced and pushed out of the chamber by the new recharged magma in the Taihe MZ (She et al., 2014). This is consistent with most of apatites of the Taihe MZ and UZ have very low Cl content (Fig. 4a–b).

A major recharge of magma with high water content at the base of the Cycle VI of the MZ may result in the slightly Cl-enriched in the apatite of the Cycle VI (Fig. 4b). Howarth et al. (2013) suggested that fractional crystallization of anhydrous minerals at depth below the Panzhihua magma chamber leads to an increase in H₂O content of residual magma. Thus, the magma of the Taihe intrusion evolving in a deep-seated magma chamber not only becomes Fe-Ti-enriched but also has high water content due to fractional crystallization of mafic silicates and chromite (She et al., 2014, 2015). A trend of decreasing Cl content in apatite within Cycle VI indicates that the water fugacity decrease gradually in an open magma plumbing system (Fig. 4b).

5.2. Crystallization order of minerals: geochemical constraints

The stratigraphic variation of mineral modes within the cyclic units of the Taihe MZ suggests that clinopyroxene together with apatite and Fe-Ti oxides may crystallize before plagioclase (Fig. 2). However, the modal criteria cannot be used unambiguously to constrain the order of mineral appearance of cumulus rocks (Means and Park, 1994; McBirney and Hunter, 1995). Mineral crystallization can result from

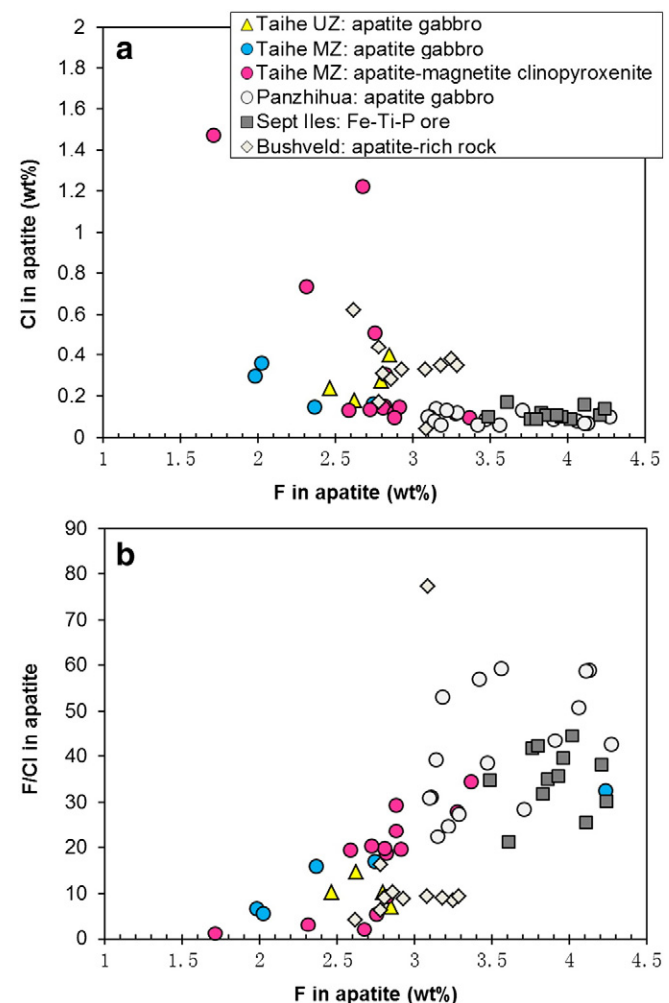


Fig. 6. Binary plots of apatite from the Taihe MZ and UZ: (a) Cl content versus F content of apatite (b) F/Cl ratio versus F content of apatite.

some factors including compositions of parental magma and intensive parameters (Pang et al., 2010; Namur et al., 2010). Thus, the timing of mineral appearance can be constrained by compositional variations in minerals.

Sr is compatible in plagioclase ($D_{\text{Sr}}^{\text{Pla/Liq}} = 1.7$, Aigner-Torres et al., 2007) and apatite ($D_{\text{Sr}}^{\text{Ap/Liq}} = 1.37$, Prowatke and Klemme, 2006), and incompatible in clinopyroxene, olivine and Fe-Ti oxides (Nielsen et al., 1992; Hart and Dunn, 1993). Therefore, abundant crystallization of either of plagioclase and apatite would induce Sr depletion of the other. As shown in Fig. 10, the extensively negative Sr anomalies of the magma in equilibrium with apatite of the Panzhihua MZb demonstrate that the apatite crystallizes later than plagioclase. Song et al. (2013) also suggested that the apatite saturation has been achieved at late-stage of the differentiation of the Panzhihua intrusion after extreme fractionation of silicates and Fe-Ti oxides and the apatite gabbro occurred only in the upper part of the intrusion. This is consistent with low An_{28–54} contents of plagioclase in the apatite gabbro of the Panzhihua MZb (Xing et al., 2014). A similar model that has been proposed for apatite-rich rocks have formed after crystallization of ~70% plagioclase in a mineral assemblage of silicate and Fe-Ti oxides (Namur et al., 2010). In contrast, the calculated magma in equilibrium with apatite of the Taihe MZ has a weakly negative Sr anomaly implying that abundant plagioclases join the liquidus after apatite (Fig. 10). This is also supported by the plagioclase has relatively high An_{53–67} contents (She et al., 2014) and appears only in the upper part of the cyclic units of the Taihe MZ (Fig. 2 and Table 1).

The apatite grains from the Panzhihua MZb have the LREE-enriched and HREE-depleted patterns on the chondrite-normalized REE plots (Fig. 9, Xing et al., 2014), which can be attributed to fractional

crystallization of clinopyroxene at the lower part of the Panzhihua intrusion. This is because HREE ($D_{\text{Gd-Lu}}^{\text{Cpx/Liq}} = 0.62–0.71$) are moderately incompatible, and LREE ($D_{\text{La-Eu}}^{\text{Cpx/Liq}} = 0.05–0.46$) are strongly incompatible in clinopyroxene in basaltic magma (Hart and Dunn, 1993; Hauri et al., 1994). The REE are strongly incompatible to olivine, plagioclase and Fe-Ti oxides (Nielsen et al., 1992; Bindeman et al., 1998; Aigner-Torres et al., 2007). The normalized REE patterns of apatite from the Taihe MZ show similar LREE but more intense HREE depletion ($\text{La/Yb} = 22–52$) relative to the apatite from the Panzhihua MZb ($\text{La/Yb} = 20–27$) (Fig. 9), strongly suggesting that abundant clinopyroxenes appear before apatite in the Taihe MZ. Positive correlations of La/Yb ratio with total REE contents and Sm/Yb ratio in the apatite also indicate that early fractional crystallization of clinopyroxenes result in enrichment of LREE relative to HREE in the residual magma (Fig. 7a–b). These geochemical features are consistent with clinopyroxene is the main cumulus phase in the lower part of cyclic units of the Taihe MZ (Fig. 2 and Table 1).

Although Cawthorn (2013) suggested the high REE in apatite may be achieved through “trapped liquid shift effect”, several lines of evidence indicate that the high LREE/HREE ratio in apatite of the Taihe MZ and UZ cannot be attributed to the re-equilibration between apatite and trapped liquid. Cawthorn (2013) proposed a model that REE contents in cumulus apatite would be increased during solidification of trapped liquid due to most of the REE are incompatible in silicates and oxides except apatite. Eu also incorporates into plagioclase crystal ($D_{\text{Eu}}^{\text{Pl/Liq}} = \sim 0.87$, Aigner-Torres et al., 2007), relatively less Eu than the other REE partitions into apatite can result in a large negative Eu anomaly of “final apatite” (Cawthorn, 2013). In contrast, in the Taihe MZ and UZ, most of apatites have weakly negative Eu anomalies in the normalized

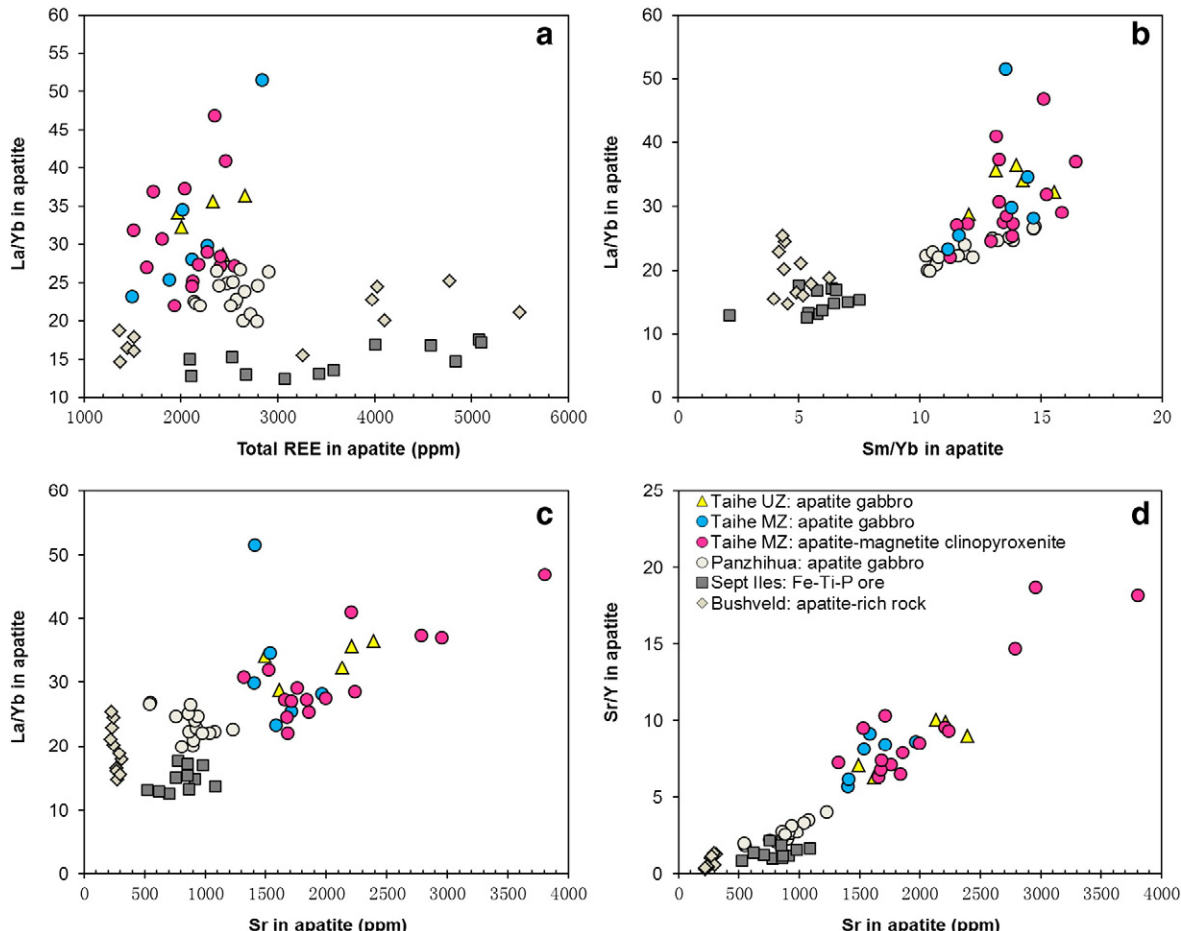


Fig. 7. Binary plots of apatite from the Taihe MZ and UZ: (a) Total REE versus La/Yb ratio; (b) Sm/Yb ratio versus La/Yb ratio; (c) Sr versus La/Yb ratio; (d) Sr versus Sr/Y ratio. The data of apatite from the Panzhihua, the Sept Iles and the Bushveld intrusions are from Xing et al. (2014); Tollari et al. (2008), and Van Tongeren and Mathez (2012), respectively.

patterns (Fig. 9). The values of Eu/Eu* of gabbros range from 0.84 to 1.02, which is close to that of apatite-magnetite clinopyroxenites (Eu/Eu* = 0.85–1.10). Similarly, Sr is compatible in plagioclase and apatite, but strongly incompatible in clinopyroxene, olivine and Fe-Ti oxides. According to the model proposed by Cawthorn (2013), the Sr in trapped liquid would partition into plagioclase resulting in negative Sr anomalies in “final apatite”. However, as shown in Fig. 10, the apatite of the Taihe MZ and UZ has weakly negative Sr anomalies. These features suggest that high Sr content and LREE/HREE ratio in apatite of the Taihe intrusion cannot be attributed to a “trapped liquid shift effect” proposed by Cawthorn (2013). Moreover, there is no evidence to indicate presence of abundant trapped liquids in the Taihe intrusion.

Apatite and Fe-Ti oxide are always closely associated and they are a subordinate phase with a poikilitic habit (Fig. 3a–b), suggesting that the apatite and Fe-Ti oxides have crystallized simultaneously after clinopyroxene. It is also noted that some fine-grains apatite and Fe-Ti oxide are enclosed by clinopyroxene (Fig. 3c–d), indicating that small amounts of apatite and Fe-Ti oxide may crystallize early. Thus, the order of crystallization in the Taihe MZ is clinopyroxene (\pm olivine), followed by Fe-Ti oxides and apatite, and then plagioclase.

5.3. Early crystallization of apatite

The crystallization order of the Taihe MZ can be compared with the Panzhihua and Hongge intrusions, in which appearance order of minerals is Fe-Ti oxides → clinopyroxene and olivine → plagioclase → apatite (Pang et al., 2008b, 2009; Luan et al., 2014). The crystallization order of the Baima and Sept Iles intrusions is olivine and plagioclase → Fe-Ti

oxides → clinopyroxene → apatite (Namur et al., 2010; Liu et al., 2014). In contrast to these intrusions, apatite crystallizes early in the Taihe MZ.

REE are strongly partitioned into the apatite crystal ($D_{\text{REE}}^{\text{Ap/Liq}} = 12$ –20, Bedard, 2001), and incompatible to silicates and oxides (Nielsen et al., 1992; Bindeman et al., 1998; Hart and Dunn, 1993). According to the typical mineral assemblage (50 modal% clinopyroxene, 40 modal% Fe-Ti oxides and 10 modal% apatite) in the lower part of the cyclic units of the Taihe MZ, the $D_{\text{REE}}^{\text{bulk}}$ can be calculated to close to 1.25–2. Thus, the REE content in the residual magma would decrease when apatite saturation had been achieved. Several reversals of total REE content in the apatite from the Taihe MZ and UZ (Fig. 4c) suggest that early crystallization of apatite lowers dramatically REE concentration in the magma during further differentiation. Moreover, appearance of abundant apatites in the lower part of the cyclic units of the Taihe MZ also results in decrease of phosphorus in the residual magma and absence of apatite in the gabbro of the Cycles II and III (Fig. 2 and Table 1). However, the apatite from most of stratigraphic levels displays small variation of Sr content, except for the significant Sr reversal in the Cycle VI (Fig. 4d). This is because Sr is weakly compatible in apatite and plagioclase ($D_{\text{Sr}}^{\text{Ap/Liq}} = 1.37$, $D_{\text{Sr}}^{\text{Pla/Liq}} = 1.7$, Prowatke and Klemme, 2006; Aigner-Torres et al., 2007). The proportion of apatite and plagioclase do not cause evident variation of Sr in the residual magma. The reversal of Sr within the Cycle VI may result from abundant apatites and plagioclases crystallized from a highly evolved magma derived from the deep-seated magma chamber (She et al., 2014). Like Sr, the variation of V in apatite shows a narrow range in the stratigraphic levels due to incompatible behavior of V in apatite (Fig. 4e). Two rough trends of decreasing V in apatite within the Cycles II and IV upwards (Fig. 4e) may

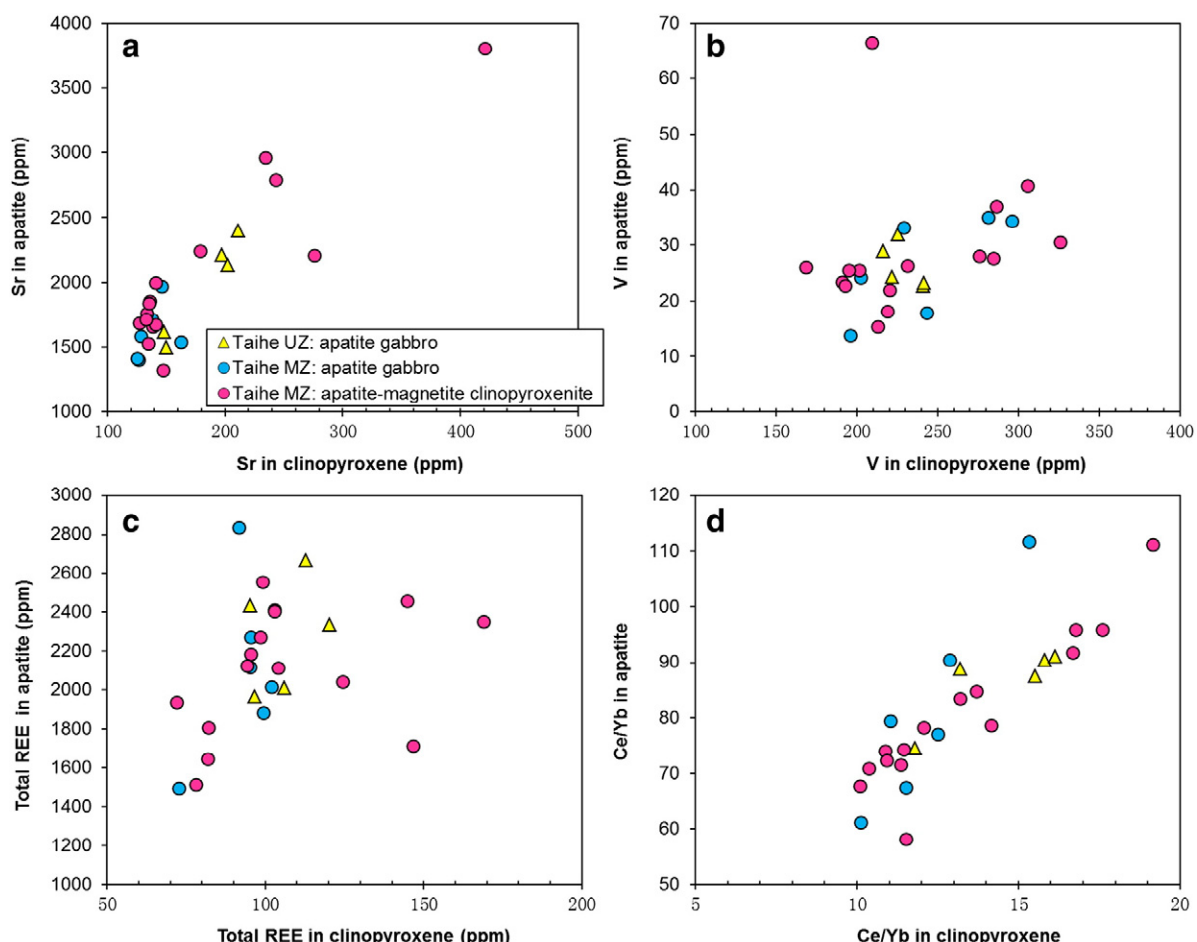


Fig. 8. Binary plots between clinopyroxene and apatite from the Taihe MZ and UZ: (a) Sr in clinopyroxene versus Sr in apatite; (b) V in clinopyroxene versus V in apatite; (c) total REE in clinopyroxene versus Total REE in apatite; (d) Ce/Yb ratio in clinopyroxene versus Ce/Yb ratio in apatite. The data of the clinopyroxene are from She et al. (2014).

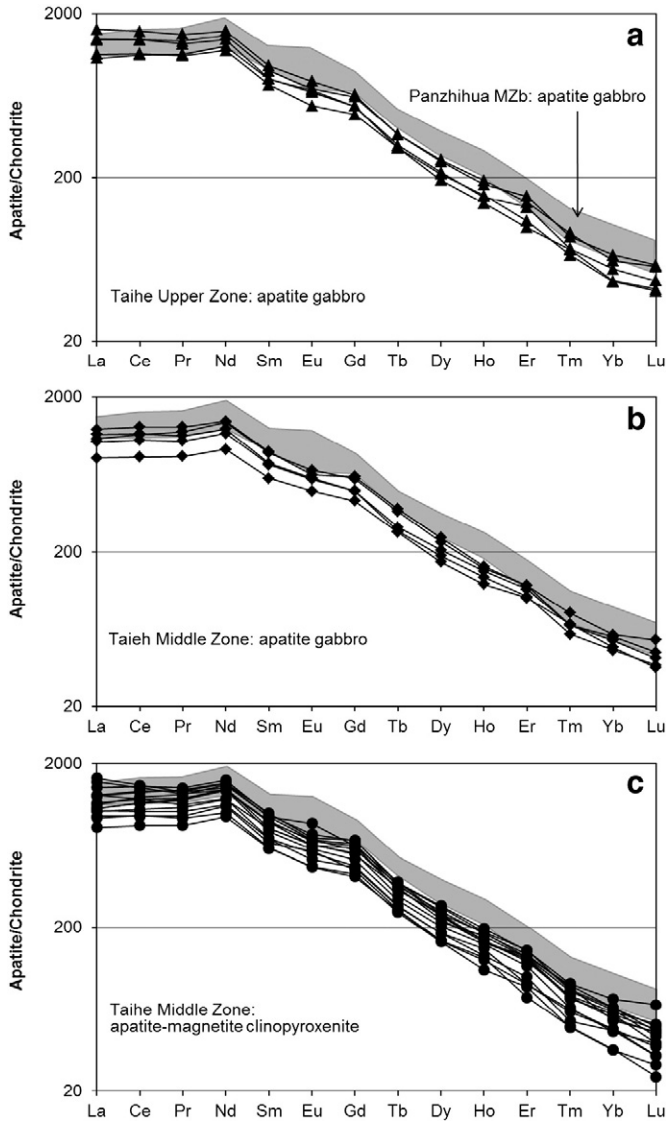


Fig. 9. Chondrite-normalized REE patterns of apatite of the Taihe MZ and UZ. The compositions of apatite of the Panzhihua MZb are from Xing et al. (2014). The chondrite REE values are from Sun and McDonough (1989).

be resulted from crystallization of abundant Fe-Ti oxides which lowers the V content in the residual magma.

Crystallization of apatite was mainly influenced by the composition of melts (Cawthorn and Walsh, 1988; Toplis et al., 1994; Tollari et al., 2006). Phosphorus is incompatible in silicate minerals and Fe-Ti oxide, the P content of the residual magma thus starts to increase with further differentiation of basaltic magma. The saturation of magma in apatite did not occur until the Upper Zone of the Skaergaard intrusion, in which the residual magma contained ~1.3–1.7 wt% P_2O_5 (McBirney and Nakamura, 1973; McBirney and Naslund, 1990). Cawthorn and Walsh (1988) estimated that the magma has ~1.3 wt% P_2O_5 when apatite saturated in the Upper Zone of the Bushveld Complex. The P_2O_5 saturation content of magma of the upper part of the Panzhihua intrusion is about 1.35 wt% according to the MELTS program calculation (Song et al., 2013). Therefore, a high degree of differentiation can result in P_2O_5 enrichment in residual magma and trigger saturation of apatite. Moreover, the experimental studies demonstrated that magnetite saturation has been delayed due to phosphorus destabilized magnetite and reacted with Fe^{3+} to form the $P-Fe^{3+}$ complexes (Gwinn and Hess, 1993; Toplis et al., 1994). Thus, the high Fe^{3+} content and further differentiation of parental magma may play an

important role to promote phosphorus enrichment in the magma of the Taihe MZ.

In the lower part of cyclic units of the Taihe MZ, apatite grains are closely coexisting with cumulus clinopyroxene (Fig. 3) suggesting that the apatite saturation may be related with fractional crystallization of clinopyroxene. As discussed above, apatite saturation has been achieved after clinopyroxene in the Taihe MZ. Thus it can be concluded that phosphorus content in the residual magma would be elevated after abundant clinopyroxenes becomes liquidus phase. The magma in equilibrium with apatite from the Taihe MZ is evidently depleted in HREE relative to LREE (Fig. 10), indicating that the crystallization of clinopyroxene elevates significantly concentration of incompatible elements in the residual magma. It is also noted that the Fe-Ti oxides are always associated with apatite suggesting that they are saturated

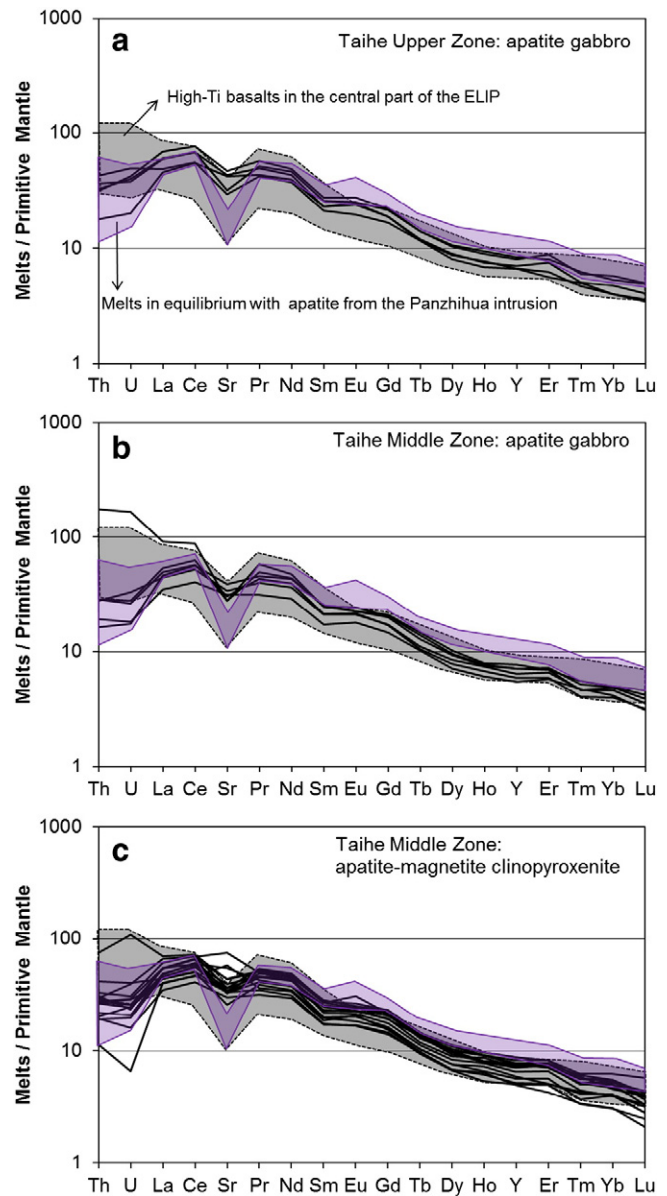


Fig. 10. Normalized trace element patterns of the calculated melts in equilibrium with apatite from the Taihe MZ and UZ. The apatite-liquid partition coefficients used for this calculation are after Watson and Green (1981), Prowatke and Klemme (2006) and Bedard (2001). The primitive mantle values are from Sun and McDonough (1989). The violet shapes show the melt compositions in equilibrium with apatite of the Panzhihua MZb (Xing et al., 2014). The gray regions indicate Emeishan high-Ti basalts after Xu et al. (2001); Xiao et al. (2004); Song et al. (2008) and Qi and Zhou (2008).

almost simultaneously (Fig. 3). Tollari et al. (2006) suggested that the P_2O_5 content of magma in apatite saturation is a function of temperature, SiO_2 and CaO contents of basaltic magma. When abundant clinopyroxenes and Fe-Ti oxides become the liquidus phases, the SiO_2 content of the magma would be elevated sharply. This process can result in the P_2O_5 content required for apatite saturation in the magma is markedly decreasing (Tollari et al., 2006). In addition, crystallization of Fe-Ti oxides can decrease the solubility of phosphorus in basaltic magma (Toplis et al., 1994). Thus, early saturation of apatite in the Taihe MZ can be ascribed to crystallization of abundant clinopyroxenes and Fe-Ti oxides.

5.4. Implications for the origin of apatite-rich Fe-Ti oxide ore

A variety of mechanisms have been proposed to explain the formation of apatite-rich oxide ores in layered intrusions (Philpotts, 1967; Cawthorn and McCarthy, 1980; Reynolds, 1985; Tegner et al., 2006). The critical question centers on whether Fe-Ti oxides and apatite are precipitated directly from magmas, or from a Fe-Ti-P-rich liquid separated immiscibly from Si-rich magma.

Liquid-liquid immiscibility implies that interstitial textural relationships between the Fe-Ti oxides (\pm apatite) and silicates would indicate that the dense Fe-Ti-(P)-rich melt percolated through the silicate crystal mush to form Fe-Ti-(P) oxide ores. The apatite and Fe-Ti oxides are the

result of solidification of the immiscible melts (Reynolds, 1985; Zhou et al., 2005; Wang and Zhou, 2013). In the apatite-rich disseminated ores of the Taihe MZ, clinopyroxene is a main phase with a cumulus texture, whereas the subordinate Fe-Ti oxides and apatite have an intercumulus habit (Fig. 3a–b). The cumulus origin for the clinopyroxene indicates that it cannot crystallize from an immiscible Fe-rich melt, although some experimental studies showed that minor silicate minerals can crystallize from the Fe-rich liquids (Lester et al., 2013). Sc is compatible in clinopyroxene and Fe-Ti oxides (Hart and Dunn, 1993; Hauri et al., 1994; Klemme et al., 2006) but incompatible in olivine, plagioclase and apatite (Nielsen et al., 1992; Bindeman et al., 1998). Thus, fractional crystallization of clinopyroxene and Fe-Ti oxides can result in decreasing Sc in magma. The negative correlation between Sc and total REE contents in clinopyroxene from the Taihe MZ (Fig. 11a) suggests that REE in magma increase with increasing amount of clinopyroxene. Moreover, Ce/Yb ratio is negatively correlated with Sc in the clinopyroxene (Fig. 11b), indicating that higher LREE relative to HREE in the magma can result from fractionation of clinopyroxene (Hart and Dunn, 1993; Hauri et al., 1994). Such the correlations suggest that the clinopyroxene has crystallized continuously from the ferrobasaltic parental magma of the Taihe MZ.

A number of experimental studies demonstrated that immiscible Fe-rich melts not only are enriched unusually in Fe, P and Ti, but also highly enriched in Sr, Th, U, REE, Zr, Hf, Nb and Ta (Shearer et al., 2001; Veksler et al., 2006, 2007; Charlier and Grove, 2012; Lester et al., 2013). Moreover, it is different in composition of apatite which originated from the immiscible Fe-rich liquid and the conjugate Si-rich liquid, respectively (Van Tongeren and Mathez, 2012). If apatite formed from a Fe-rich immiscible melt, it is supposed to disequilibrium in geochemical composition with clinopyroxene which crystallized from a normally ferrobasaltic magma. However, there are positive correlations between Sr, V and total REE contents, and Ce/Yb ratio in apatite and in clinopyroxene from apatite gabbros and apatite-magnetite clinopyroxenites in the Taihe MZ (Fig. 8), indicating geochemical equilibrium among these phases. Therefore, it seems that both apatite and clinopyroxene may crystallize from the same ferrobasaltic magma rather than two distinguishing melts. Furthermore, negative correlation of Ce/Yb with Sc in the clinopyroxene indicates that the magma becomes LREE enrichment with further differentiation (Fig. 11b), consistent with the positive correlations of La/Yb with total REE and Sm/Yb in the apatite (Fig. 7a–b). La/Yb and Sr/Y ratios in the apatite are positively correlated with Sr contents (Fig. 7c–d) also suggesting that the apatite crystallizes continuously from the magma of the Taihe MZ. It is therefore unlikely that the apatite forms from an immiscible Fe-Ti-P-enriched melt.

The experimental studies demonstrated that phosphorous can promote iron enrichment in a basaltic magma because it destabilized magnetite (Gwinn and Hess, 1993; Toplis et al., 1994). However, high fO_2 condition would result in the crystallization of Fe-Ti oxides, which in turn prevents iron enrichment (Toplis and Carroll, 1995). The ratio of Eu^{2+}/Eu^{3+} in magma and apatite is greatly dependent upon oxygen fugacity condition (Drake, 1975). Apatite generally accepts Eu^{3+} into its structure but excludes Eu^{2+} , thus Eu anomaly in apatite can be used to infer the redox state of the magma. Low oxygen fugacity results in low Eu^{3+} content in magma, leading to limited Eu partitioning into apatite, thus creating a strong negative Eu anomaly in apatite (Sha and Chappell, 1999; Belousova et al., 2001, 2002). The absence of negative Eu anomalies in apatite of the Taihe MZ and UZ (Fig. 9) suggests that it crystallizes from an oxidizing magma. Thus it can be concluded that the high fO_2 condition and high Fe and Ti contents lead to saturation of Fe-Ti oxides in the magma. The crystallization of abundant clinopyroxenes and Fe-Ti oxides can trigger saturation in apatite (Toplis et al., 1994; Tollari et al., 2006). Early crystallization and accumulation of these minerals form the apatite-rich oxide ores in the lower part of the cyclic units of the Taihe MZ.

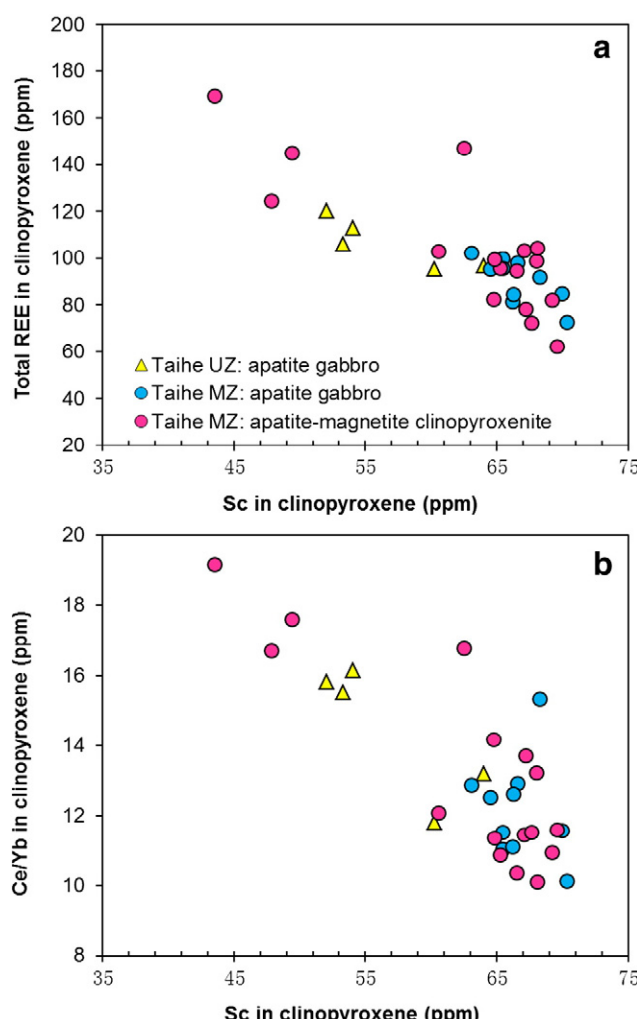


Fig. 11. Binary plots of clinopyroxene from the Taihe MZ and UZ: (a) Binary plot of Sc versus total REE of clinopyroxene; (b) binary plot of Sc versus Ce/Yb ratio of clinopyroxene. The data of the clinopyroxene are from She et al. (2014).

6. Conclusions

Our results indicate that the Taihe MZ and UZ crystallized from a hydrous ferrobasaltic parental magma. The order of crystallization in the Taihe MZ is: clinopyroxene (\pm olivine), followed by Fe-Ti oxides and apatite, and then plagioclase. The timing of apatite saturation is controlled by the phosphorus content in the parental magma. The crystallization of abundant clinopyroxenes and high Fe^{3+} contents in the magma promote phosphorus enrichment. High oxygen fugacity and elevated Fe and Ti contents trigger crystallization of Fe-Ti oxides. Decline of SiO_2 and iron contents in the magma resulted from saturation of clinopyroxene and Fe-Ti oxides is responsible for the early crystallization of apatite together with oxides. Compositional equilibrium between apatite and clinopyroxene indicate that these phases formed from the same ferrobasaltic magma. Early crystallization and accumulation of apatite, Fe-Ti oxides and clinopyroxene resulted in the formation of the apatite-rich disseminated oxide ores in the lower half in each cyclic unit of the Taihe MZ.

Acknowledgment

We thank Prof. Guo-Fu Zhou and Mr. Liang Li for the EPMA and LA-ICPMS analysis, respectively. Mr. Yu Wei is appreciated for field assistance. This study was funded by the National Basic Research Program of China (2012CB416804), CAS/SAFEA International Partnership Program for Creative Research Teams (KZZD-EW-TZ-20), 12th Five-Year-Plan project of State Key Laboratory of Ore-deposit Geochemistry, Chinese Academy of Sciences (SKLODG-ZY125-06) and NSFC (40730420) to Xie-Yan Song.

References

- Aigner-Torres, M., Blundy, J., Ulmer, P., Pettke, T., 2007. Laser ablation ICPMS study of trace element partitioning between plagioclase and basaltic melts: an experimental approach. *Contrib. Mineral. Petrol.* 153, 647–667.
- Ashwal, L.D., 2010. The temporality of anorthosites. *Can. Mineral.* 48, 711–728.
- Bai, Z.-J., Zhong, H., Naldrett, A.J., Zhu, W.-G., Xu, G.-W., 2012. Whole-rock and mineral composition constraints on the genesis of the giant Hongge Fe-Ti-V oxide deposit in the Emeishan large igneous province, southwest China. *Econ. Geol.* 107, 507–524.
- Bedard, J.H., 2001. Parental magmas of the Nain Plutonic Suite anorthosites and mafic cumulates: a trace element modelling approach. *Contrib. Mineral. Petrol.* 141, 747–771.
- Belousova, E., Walters, S., Griffin, W., O'Reilly, S.Y., 2001. Trace-element signatures of apatites in granitoids from the Mt Isa Inlier, northwestern Queensland. *Aust. J. Earth Sci.* 48, 603–619.
- Belousova, E., Griffin, W., O'Reilly, S.Y., Fisher, N., 2002. Apatite as an indicator mineral for mineral exploration: trace-element compositions and their relationship to host rock type. *J. Geochem. Explor.* 76, 45–69.
- Bindeman, I.N., Davis, A.M., Drake, M.J., 1998. Ion microprobe study of plagioclase-basalt partition experiments at natural concentration levels of trace elements. *Geochim. Cosmochim. Acta* 62, 1175–1193.
- Botcharnikov, R.E., Almeev, R.R., Koepke, J., Holtz, F., 2008. Phase relations and liquid lines of descent in hydrous ferrobasalt—implications for the Skaergaard intrusion and Columbia River flood basalts. *J. Petrol.* 49, 1687–1727.
- Boudreau, A.E., McCallum, I.S., 1989. Investigations of the Stillwater Complex: part 4. Apatite as indicators of evolving fluid composition. *Contrib. Mineral. Petrol.* 102, 138–153.
- Boudreau, A.E., Mathez, E.A., McCallum, I.S., 1986. Halogen geochemistry of the Stillwater and Bushveld Complexes: evidence for transport of the platinum-group elements by Cl-rich fluids. *J. Petrol.* 27, 967–986.
- Boudreau, A.E., Love, C., Prendergast, M.D., 1995. Halogen geochemistry of the Great Dyke, Zimbabwe. *Contrib. Mineral. Petrol.* 122, 289–300.
- Cawthorn, R.G., 2013. Rare earth element abundances in apatite in the Bushveld Complex—a consequence of the trapped liquid shift effect. *Geology* 41, 603–606.
- Cawthorn, R.G., 2015. The Bushveld Complex, South Africa. In: Charlier, et al. (Eds.), *Layered Intrusions*. Springer Geology, pp. 517–588.
- Cawthorn, R.G., McCarthy, T.S., 1980. Variations in Cr content of magnetite from the upper zone of the Bushveld Complex. Evidence for heterogeneity and convection currents in magma chambers. *Earth Planet. Sci. Lett.* 46, 335–343.
- Cawthorn, R.G., Walsh, K.L., 1988. The use of phosphorus contents in yielding estimates of the proportion of trapped liquid in cumulates of the Upper Zone of the Bushveld Complex. *Mineral. Mag.* 52, 81–89.
- Charlier, B., Grove, T.L., 2012. Experiments on liquid immiscibility along tholeiitic liquid lines of descent. *Contrib. Mineral. Petrol.* 164, 27–44.
- Chu, M.-F., Wang, K.-L., Griffin, W.L., Chung, S.-L., O'Reilly, S.Y., Pearson, N.J., Iizuka, Y., 2009. Apatite composition: tracing petrogenetic processes in Transhimalayan granitoids. *J. Petrol.* 50, 1829–1855.
- Chung, S.-L., Jahn, B.M., 1995. Plume-lithosphere interaction in generation of the Emeishan flood basalts at the Permian-Triassic boundary. *Geology* 23, 889–892.
- Dong, H., Xing, C.-M., Wang, C.Y., 2013. Textures and mineral compositions of the Xinjie layered intrusion, SW China: implications for the origin of magnetite and fractionation process of Fe-Ti-rich basaltic magmas. *Geosci. Front.* 4, 503–515.
- Drake, M., 1975. The oxidation state of europium as an indicator of oxygen fugacity. *Geochim. Cosmochim. Acta* 39, 55–64.
- Duchesne, J.C., 1999. Fe-Ti deposits in Rogaland anorthosites (South Norway): geochemical characteristics and problems of interpretation. *Mineral. Deposita* 34, 182–198.
- Dymek, R.F., Owens, B.E., 2001. Petrogenesis of apatite-rich rocks (nelsonites and oxidapatite gabbronorites) associated with massif anorthosites. *Econ. Geol.* 96, 797–815.
- Eales, H.V., Cawthorn, R.G., 1996. The Bushveld complex. In: Cawthorn, R.G. (Ed.), *Layered Intrusions*. Elsevier, Amsterdam, pp. 181–232.
- Ganino, C., Arndt, N.T., Zhou, M.-F., Gaillard, F., Chauvel, C., 2008. Interaction of magma with sedimentary wall rock and magnetite ore genesis in the Panzhihua mafic intrusion, SW China. *Mineral. Deposita* 43, 677–694.
- Ganino, C., Harris, C., Arndt, N.T., Prevec, S.A., Howarth, G.H., 2013. Assimilation of carbonate country rock by the parent magma of the Panzhihua Fe-Ti-V deposit (SW China): evidence from stable isotopes. *Geosci. Front.* 4, 547–554.
- Goldoff, B., Webster, J.D., Harlov, D.E., 2012. Characterization of fluor-chlorapatites by electron probe microanalysis with a focus on time-dependent intensity variation of halogens. *Am. Mineral.* 97, 1103–1115.
- Gwinn, R., Hess, P.C., 1993. The role of phosphorus in rhyolitic liquids as determined from the homogenous iron redox equilibrium. *Contrib. Mineral. Petrol.* 106, 129–141.
- Hart, S.R., Dunn, T., 1993. Experimental cpx/melt partitioning of 24 trace elements. *Contrib. Mineral. Petrol.* 113, 1–8.
- Hauri, E.H., Wagner, T.P., Grove, T.L., 1994. Experimental and natural partitioning of Th, U, Pb and other trace elements between garnet, clinopyroxene and basaltic melts. *Chem. Geol.* 117, 149–166.
- Hei, H.-X., Luo, Z.-H., Cheng, J.-H., Qiu, Y.-R., Deng, J.-F., Li, J., Vikentyev, I.V., 2015. Fluid dynamics model of mafic magmatic metallogenesis system in Panxian area. *Earth Sci. Frontiers* 22, 333–347 (in Chinese).
- Higgins, M.D., Doig, R., 1981. The Sept Iles anorthosite complex: Field relationships, geochronology and petrology. *Can. J. Earth Sci.* 18, 561–573.
- Hoskin, P.W., Kinny, P.D., Wyborn, D., Chappell, B.W., 2000. Identifying accessory mineral saturation during differentiation in granitoid magmas: an integrated approach. *J. Petrol.* 41, 1365–1396.
- Hou, T., Zhang, Z.-C., Pirajno, F., 2012. A new metallogenetic model of the Panzhihua giant V-Ti-iron oxide deposit (Emeishan Large Igneous Province) based on high-Mg olivine-bearing wehrlite and new field evidence. *Int. Geol. Rev.* 54, 1721–1745.
- Hou, T., Zhang, Z.-C., Encarnacion, J., Santosh, M., Sun, Y., 2013. The role of recycled oceanic crust in magmatism and metallogeny: Os-Sr-Nd isotopes, U-Pb geochronology and geochemistry of picritic dykes in the Panzhihua giant Fe-Ti oxide deposit, central Emeishan large igneous province, SW China. *Contrib. Mineral. Petrol.* 165, 805–822.
- Howarth, G.H., Prevec, S.A., 2013. Trace element, PGE, and Sr-Nd isotope geochemistry of the Panzhihua mafic layered intrusion, SW China: constraints on ore-forming processes and evolution of parent magma at depth in a plumbing-system. *Geochim. Cosmochim. Acta* 120, 459–478.
- Howarth, G.H., Prevec, S.A., Zhou, M.-F., 2013. Timing of Ti-magnetite crystallisation and silicate disequilibrium in the Panzhihua mafic layered intrusion: implications for ore-forming processes. *Lithos* 170, 73–89.
- Klemme, S., Gunther, D., Hametner, K., Prowatke, S., Zack, T., 2006. The partitioning of trace elements between ilmenite, ulvöspinel, armalcolite and silicate melts with implications for the early differentiation of the moon. *Chem. Geol.* 234, 251–263.
- Kolker, A., 1982. Mineralogy and geochemistry of Fe-Ti oxide and apatite (nelsonite) deposits and evaluation of the liquid immiscibility hypothesis. *Econ. Geol.* 77, 1146–1158.
- Lester, G.W., Kyser, T.K., Clark, A.H., Layton-Mathews, D., 2013. Trace element partitioning between immiscible silicate melts with H_2O , P, S, F, and Cl. *Chem. Geol.* 357, 178–185.
- Lister, G.F., 1966. The composition and origin of selected iron-titanium deposits. *Econ. Geol.* 61, 275–310.
- Liu, D., Shen, F.-K., Zhang, G.-Z., 1985. Layered intrusions of the Panxian area, Sichuan province. In: Zhang, Y.X. (Ed.), *Corpus of the Panxian Paleorift Studies in China*. Geological Press, Beijing, pp. 85–118 (in Chinese).
- Liu, Y.-S., Hu, Z.-C., Gao, S., Günther, D., Xu, J., Gao, C., Chen, H., 2008. In situ analysis of major and trace elements of anhydrous minerals by LA-ICP-MS without applying an internal standard. *Chem. Geol.* 257, 34–43.
- Liu, P.-P., Zhou, M.-F., Wang, C.Y., Xing, C.-M., Gao, J.-F., 2014. Open magma chamber processes in the formation of the Permian Baima mafic-ultramafic layered intrusion, SW China. *Lithos* 184–187, 194–208.
- Luan, Y., Song, X.-Y., Chen, L.-M., Zheng, W.-Q., Zhang, X.-Q., Yu, S.-Y., She, Y.-W., Tian, X.-L., Ran, Q.-Y., 2014. Key factors controlling the accumulation of the Fe-Ti oxides in the Hongge layered intrusion in the Emeishan Large Igneous Province, SW China. *Ore Geol. Rev.* 57, 518–538.
- Luo, W.-J., Zhang, Z.-C., Santosh, M., Hou, T., Huang, H., Zhu, J., Wang, X., Fu, X., 2014. Petrology and geochemistry of Permian mafic-ultramafic intrusions in the Emeishan large igneous province, SW China: insight into the ore potential. *Ore Geol. Rev.* 56, 258–275.
- Mathez, E.A., Webster, J.D., 2005. Partitioning behavior of chlorine and fluorine in the system apatite-silicate melt-fluid. *Geochim. Cosmochim. Acta* 69, 1275–1286.
- McBirney, A.R., Hunter, R.H., 1995. The cumulus paradigm reconsidered. *J. Geol.* 103, 114–122.

- McBirney, A.R., Nakamura, Y., 1973. Immiscibility in late stage magmas of the Skaergaard intrusion. *Carnegie Inst. Yearb.* 72, 348–352.
- McBirney, A.R., Naslund, H.R., 1990. The differentiation of the Skaergaard Intrusion. A discussion of Hunter and Sparks. *Contrib. Mineral. Petro.* 104, 235–240.
- McLellan, J.M., Selleck, B.W., Hamilton, M.A., Bickford, M.E., 2010. Late- to post-tectonic setting of some major Proterozoic anorthosite–mangerite–charnockite–granite (AMCG) suites. *Can. Mineral.* 48, 729–750.
- Means, W.D., Park, Y., 1994. New experimental approach to understanding igneous texture. *Geology* 22, 323–326.
- Miles, A.J., Graham, C.M., Hawkesworth, C.J., Gillespie, M.R., Hinton, R.W., 2013. Evidence for distinct stages of magma history recorded by the compositions of accessory apatite and zircon. *Contrib. Mineral. Petro.* 166, 1–19.
- Namur, O., Charlier, B., Toplis, M.J., Higgins, M.D., Liégeois, J.P., Vander Auwera, J., 2010. Crystallization sequence and magma chamber processes in the ferrobasaltic Sept Iles layered intrusion. *Canada. J. Petrol.* 51, 1203–1236.
- Nash, W.P., 1976. Fluorine, chlorine and OH-bearing minerals in the Skaergaard intrusion. *Am. J. Sci.* 276, 546–557.
- Naslund, H.R., 1983. The effect of oxygen fugacity on liquid immiscibility in iron-bearing silicate melts. *Am. J. Sci.* 283, 1034–1059.
- Nielsen, R.L., Gallahan, W.E., Newberger, F., 1992. Experimentally determined mineral–melt partition coefficients for Sc, Y and REE for olivine, orthopyroxene, pigeonite, magnetite and ilmenite. *Contrib. Mineral. Petro.* 110, 488–499.
- Pang, K.-N., Zhou, M.-F., Lindsley, D., Zhao, D., Malpas, J., 2008a. Origin of Fe-Ti oxide ores in mafic intrusions: evidence from the Panzhihua Intrusion, SW China. *J. Petrol.* 49, 295–313.
- Pang, K.-N., Li, C., Zhou, M.-F., Ripley, E.M., 2008b. Abundant Fe-Ti oxide inclusions in olivine from the Panzhihua and Hongge layered intrusions, SW China: evidence for early saturation of Fe-Ti oxides in ferrobasaltic magma. *Contrib. Mineral. Petro.* 156, 307–321.
- Pang, K.-N., Li, C., Zhou, M.-F., Ripley, E.M., 2009. Mineral compositional constraints on petrogenesis and oxide ore genesis of the late Permian Panzhihua layered gabbroic intrusion, SW China. *Lithos* 110, 199–214.
- Pang, K.-N., Zhou, M.-F., Qi, L., Shellnutt, J.G., Wang, C.Y., Zhao, D.-G., 2010. Flood basalt-related Fe-Ti oxide deposits in the Emeishan large igneous province, SW China. *Lithos* 119, 123–136.
- Philpotts, A.R., 1967. Origin of certain iron-titanium oxide and apatite rocks. *Econ. Geol.* 62, 303–315.
- Prowatke, S., Klemme, S., 2006. Trace element partitioning between apatite and silicate melts. *Geochim. Cosmochim. Acta* 70, 4513–4527.
- Qi, L., Zhou, M.-F., 2008. Platinum-group elemental and Sr-Nd-Os isotopic geochemistry of Permian Emeishan flood basalts in Guizhou Province, SW China. *Chem. Geol.* 248, 83–103.
- Reynolds, I.M., 1985. Contrasted mineralogy and textural relationships in the uppermost titaniferous magnetite layers of the Bushveld Complex in the Bierkraal area north of Rustenburg. *Econ. Geol.* 80, 1027–1048.
- Sha, L.K., Chappell, B.W., 1999. Apatite chemical composition, determined by electron microprobe and laser-ablation inductively coupled plasma mass spectrometry, as a probe into granite petrogenesis. *Geochim. Cosmochim. Acta* 63, 3861–3881.
- She, Y.-W., Yu, S.-Y., Song, X.-Y., Chen, L.-M., Zheng, W.-Q., Luan, Y., 2014. The formation of P-rich Fe-Ti oxide ore layers in the Taihe layered intrusion, SW China: implications for magma-plumbing system process. *Ore Geol. Rev.* 57, 539–559.
- She, Y.-W., Song, X.-Y., Yu, S.-Y., He, H.-L., 2015. Variations of trace element concentration of magnetite and ilmenite from the Taihe layered intrusion, Emeishan large igneous province, SW China: implications for magmatic fractionation and origin of Fe-Ti-V oxide ore deposits. *J. Asian Earth Sci.* 113, 1117–1131.
- Shearer, C.K., Papike, J.J., Spilde, M.N., 2001. Trace-element partitioning between immiscible lunar melts: an example from naturally occurring lunar melt inclusions. *Am. Mineral.* 86, 238–246.
- Shellnutt, J.G., Zhou, M.-F., 2008. Permian, rifting related fayalite syenite in the Panxi region, SW China. *Lithos* 101, 54–73.
- Shellnutt, J.G., Zhou, M.-F., Chung, S.-L., 2010. The Emeishan large igneous province: advances in the stratigraphic correlations and petrogenetic and metallogenetic models. *Lithos* 119 (ix–x).
- Sisson, T.W., Grove, T.L., 1993. Experimental investigations of the role of H_2O in calc-alkaline differentiation and subduction zone magmatism. *Contrib. Mineral. Petro.* 113, 143–166.
- Song, X.-Y., Qi, H.-W., Robinson, P.T., Zhou, M.-F., Cao, Z.-M., Chen, L.-M., 2008. Melting of the subcontinental lithospheric mantle by the Emeishan mantle plume; evidence from the basal alkaline basalts in Dongchuan, Yunnan, Southwestern China. *Lithos* 100, 93–111.
- Song, X.-Y., Keays, R.-R., Xiao, L., Qi, H.-W., Ihlenfeld, C., 2009. Platinum-group element geochemistry of the continental flood basalts in the central Emeishan Large Igneous Province, SW China. *Chem. Geol.* 262, 246–261.
- Song, X.-Y., Qi, H.-W., Hu, R.-Z., Chen, L.-M., Yu, S.-Y., Zhang, J.-F., 2013. Formation of thick stratiform Fe-Ti oxide layers in layered intrusion and frequent replenishment of fractionated mafic magma: evidence from the Panzhihua intrusion, SW China. *Geochem. Geophys. Geosyst.* 14, 712–732.
- Sun, S.-S., McDonough, W.F., 1989. Chemical and isotopic systematics of oceanic basalts: implications for mantle composition and processes. In: Saunders, A.D., Norry, M.J. (Eds.), *Magmatism in the Ocean Basins*. *Geol. Soc. Lond. Spec. Publ.* vol. 42, pp. 313–345.
- Tegner, C., Cawthorn, R.G., Kruger, F.J., 2006. Cyclicity in the Main and Upper Zones of the Bushveld Complex, South Africa: crystallization from a zoned magma sheet. *J. Petrol.* 47, 2257–2279.
- Tollari, N., Toplis, M.J., Barnes, S.-J., 2006. Predicting phosphate saturation in silicate magmas: an experimental study of the effects of melt composition and temperature. *Geochim. Cosmochim. Acta* 70, 1518–1536.
- Tollari, N., Barnes, S.-J., Cox, R.A., Nabil, H., 2008. Trace element concentrations in apatites from the Sept-Iles Intrusive Suite, Canada—implications for the genesis of nelsonites. *Chem. Geol.* 252, 180–190.
- Toplis, M.J., Carroll, M.R., 1995. An experimental study of the influence of oxygen fugacity on Fe-Ti oxide stability, phase relations, and mineral-melt equilibria in ferro-basaltic systems. *J. Petrol.* 36, 1137–1170.
- Toplis, M.J., Libourel, G., Carroll, M.R., 1994. The role of phosphorus in crystallisation processes of basalt: an experimental study. *Geochim. Cosmochim. Acta* 58, 797–810.
- Treloar, P.J., Colley, H., 1996. Variations in F and Cl contents in apatites from magnetite-apatite ores in northern Chile, and their ore-genetic implications. *Mineral. Mag.* 60, 285–301.
- Van Tongeren, J.A., Mathez, E.A., 2012. Large-scale liquid immiscibility at the top of the Bushveld Complex, South Africa. *Geology* 40, 491–494.
- Veksler, I.V., Dorfman, A.M., Danyushevsky, L.V., Jakobsen, J.K., Dingwell, D.B., 2006. Immiscible silicate liquid partition coefficients: implications for crystal-melt element partitioning and basalt petrogenesis. *Contrib. Mineral. Petro.* 152, 685–702.
- Veksler, I.V., Dorfman, A.M., Borisov, A.A., Wirth, R., Dingwell, D.B., 2007. Liquid immiscibility and the evolution of basaltic magma. *J. Petrol.* 48, 2187–2210.
- Von Gruenewaldt, G., 1993. Ilmenite-apatite enrichments in the Upper Zone of the Bushveld Complex: a major titanium-rock phosphate resource. *Int. Geol. Rev.* 35, 987–1000.
- Wang, C.Y., Zhou, M.-F., 2013. New textural and mineralogical constraints on the origin of the Hongge Fe-Ti-V oxide deposit, SW China. *Mineral. Deposita* 48, 787–798.
- Watson, E.B., Green, T.H., 1981. Apatite/liquid partition coefficients for the rare earth elements and strontium. *Earth Planet. Sci. Lett.* 56, 405–421.
- Webster, J.D., DeVivo, B., 2002. Experimental and modeled solubilities of chlorine in aluminosilicate melts, consequences of magma evolution, and implications for exsolution of hydrous chloride melt at Mt. Somma-Vesuvius. *Am. Mineral.* 87, 1046–1061.
- Webster, J.D., Kinzler, R.J., Mathez, E.A., 1999. Chloride and water solubility in basalt and andesite melts and implications for magmatic degassing. *Geochim. Cosmochim. Acta* 63, 729–738.
- Willmore, C.C., Boudreau, A.E., Kruger, F.J., 2000. The halogen geochemistry of the Bushveld Complex, Republic of South Africa: implications for chalcophile element distribution in the lower and critical zones. *J. Petrol.* 41, 1517–1539.
- Xiao, L., Xu, Y.-G., Mei, H.-J., Zheng, Y.-F., He, B., Pirajno, F., 2004. Distinct mantle sources of low-Ti and high-Ti basalts from the western Emeishan large igneous province, SW China: implications for plume-lithosphere interaction. *Earth Planet. Sci. Lett.* 228, 525–546.
- Xing, C.-M., Wang, C.Y., Li, C.-Y., 2014. Trace element compositions of apatite from the middle zone of the Panzhihua layered intrusion, SW China: insights into the differentiation of a P- and Si-rich melt. *Lithos* 204, 188–202.
- Xu, Y.-G., Chung, S.-L., Jahn, B.M., Wu, G., 2001. Petrologic and geochemical constraints on the petrogenesis of Permian-Triassic Emeishan flood basalts in southwestern China. *Lithos* 58, 145–168.
- Xu, Y.-G., Luo, Z.-Y., Huang, X.-L., He, B., Xiao, L., Xie, L.-W., Shi, Y.-R., 2008. Zircon U-Pb and Hf isotope constraints on crustal melting associated with the Emeishan mantle plume. *Geochim. Cosmochim. Acta* 72, 3084–3104.
- Zhang, Z.-C., Mao, J.-W., Saunders, A.D., Ai, Y., Li, Y., Zhao, L., 2009. Petrogenetic modeling of three mafic-ultramafic layered intrusions in the Emeishan large igneous province, SW China, based on isotopic and bulk chemical constraints. *Lithos* 113, 369–392.
- Zhang, X.-Q., Song, X.-Y., Chen, L.-M., Xie, W., Yu, S.-Y., Zheng, W.-Q., Deng, Y.-F., Zhang, J.-F., Gui, S.-G., 2012. Fractional crystallization and the formation of thick Fe-Ti-V oxide layers in the Baima layered intrusion, SW China. *Ore Geol. Rev.* 49, 96–108.
- Zhong, H., Zhu, W.-G., 2006. Geochronology of layered mafic intrusions from the Pan-Xi area in the Emeishan large igneous province, SW China. *Mineral. Deposita* 41, 599–606.
- Zhong, H., Campbell, I.H., Zhu, W.-G., Allen, C.M., Hu, R.-Z., Xie, L.-W., He, D.-F., 2011. Timing and source constraints on the relationship between mafic and felsic intrusions in the Emeishan large igneous province. *Geochim. Cosmochim. Acta* 75, 1374–1395.
- Zhou, M.-F., Yan, D.P., Kennedy, A.K., Li, Y., Ding, J., 2002. SHRIMP U-Pb zircon geochronological and geochemical evidence for Neoproterozoic arc-magmatism along the western margin of the Yangtze Block, South China. *Earth Planet. Sci. Lett.* 196, 51–67.
- Zhou, M.-F., Robinson, P.T., Lesher, C.M., Keays, R.R., Zhang, C.-J., Malpas, J., 2005. Geochemistry, petrogenesis and metallogenesis of the Panzhihua gabbroic layered intrusion and associated Fe-Ti-V oxide deposits, Sichuan Province, SW China. *J. Petrol.* 46, 2253–2280.
- Zhou, M.-F., Arndt, N.T., Malpas, J., Wang, C.Y., Kennedy, A.K., 2008. Two magma series and associated ore deposit types in the Permian Emeishan large igneous province, SW China. *Lithos* 103, 352–368.
- Zhou, M.-F., Chen, W.-T., Wang, C.Y., Prevec, S.A., Liu, P.-P., Howarth, G.-H., 2013. Two stages of immiscible liquid separation in the formation of Panzhihua-type Fe-Ti-V oxide deposits, SW China. *Geosci. Front.* 4, 481–502.